MICROMODEL METHOD FOR ENHANCED OIL RECOVERY; FABRICATION AND IMAGE PROCESSING

by

© Maziyar Mahmoodi

A thesis submitted to the

School of Graduate Studies

in partial fulfillment of the requirement for the degree of

Master of Engineering

Faculty of Engineering and Applied Science

Memorial University of Newfoundland

October 2017

St. John’s Newfoundland and Labrador

ABSTRACT

The number of research projects that employ microtechnology and microfluidic devices has expanded the application of this technique to more innovative fields of study over recent decades. Oil and gas production, a multidisciplinary industrial field, has benefited from the opportunities that microfluidic devices provide to study microscale processes, such as adhesion, interfacial tension (IFT) alteration and multiphase pore scale transportation. Obtaining a deeper understanding through the micromodel visualization experiments, the governing factors in large scale extraction from hydrocarbon reservoirs will be controlled efficiently.

The diversity of proposed micromodel research and the associated requirements have led researchers to develop new methodologies, materials and techniques to overcome challenges attributed to micromodel visualization experiments. This project aims to suggest alternative solutions for two main problems, model fabrication and visual data interoperation, related to the process of exploiting the micromodels in Enhanced Oil Recovery (EOR) screening studies.

First, this research tries to modify and combine the recent advances in wet etching micromodel fabrication method to offer a low-cost and efficient alternative procedure. This modified procedure offers increased flexibility in size and network pattern as well as a significant reduction in the material, time and operation costs. Next, the fabricated prototype is applied in a two-phase flow visualization study to verify the proposed features under the specified experimental conditions.

Following the fabrication of a suitable glass micromodel, this thesis will explore processing/analysis of the visual data in a micromodel experiment. In this section, an image-based computational algorithm is developed and programmed in LabVIEW. This platform

offers a graphical programming language and a vision toolbox that can be used for image processing purposes. The availability of advanced image-transform functions and the simplicity of working with LabVIEW, provide the unique opportunity to implement a sophisticated graphical-based algorithm that quantifies the visual observations during a glass micromodel test for enhanced oil recovery screening purposes. The performance of this custom algorithm is then verified by comparison of calculated data from carbonated water injection (CWI) images with absolute values derived from volumetric material balance. Through this procedure, the controlling parameters for utilized LabVIEW functions are optimized to obtain an acceptable agreement between estimated results and true values. At the final stage, the implementation of the presented algorithm in the LabVIEW and a popular commercial software are compared to highlight the advantages and disadvantages.

ACKNOWLEDGEMENTS

Looking back over the years spent earning my Master's degree, I can see many people who deserve credit for their contributions to this research throughout my graduate studies.

First of all, I would like to express my sincere gratitude to my academic advisor, Dr. Lesley James who has been a teacher with her ideas, a supporter with her patience and a friend by encouraging me all the time.

I would like to thank my family for their support and encouragement. Especially, there is an eternal appreciation towards to my mother and father, who made this experience possible.

During the program, I have had the chance to work with some great staff in our research group. They gave me supports in their way, as I needed to keep going. Therefore, I feel grateful to project managers and engineers at the Hibernian Enhanced Oil Recovery Center, especially Edison Sirpal and Shervin Ayazi.

Finally, it is my pleasure to thank Chevron Canada, Hibernia Management and Development Company (HMDC), Research and Development Corporation of Newfoundland and Labrador (RDC), Natural Sciences and Engineering Research Council of Canada (NSERC), and the Canadian Foundation for Innovation (CFI) for financial support.

TABLE OF CONTENTS

LIST OF FIGURES

LIST OF TABLES

LIST OF SYMBOLS, NOMENCLATURE OR ABBREVIATIONS

RF	Recovery Factor
EOR	Enhanced Oil Recovery
IOR	Improved Oil Recover
OIIP	Original Oil Recovery
EP_S	Microscopic Efficiency
E_S	Macroscopic Efficiency
E_D	Connected Volume
E_C	Economic Efficiency
WAG	Water Alternative Gas
TADB	Thermal Assisted Direct Bonding
CWI	Carbonated Water Injection
UT	Uncertainty Thresholded
ME	Misclassification Error

CHAPTER 1
INTRODUCTION
AND
OVERVIEW

1.1 Overview

1.1.1 Enhanced Oil Recovery

The growing global demand for hydrocarbon resources and a wide range of petroleum derivatives' applications in advanced industrial fields have been the motivation for directing investments towards the development of oil and gas production technologies [1]. Despite the adverse effect of oil price fluctuation, other factors, such as maturating current producing reservoirs and decreasing trend of new oilfield discoveries have motivated oil companies to maximize the ultimate recovery factor (RF) from oil reservoirs [2].

The techniques involved in hydrocarbon recovery can be categorized into three main phases: a) primary recovery, b) secondary recovery and c) tertiary recovery [3]. Primary recovery is defined as total produced oil by natural driving forces such as rock/liquid expansion drive, reservoir fluids (water and gas cap) drive and depletion drive [4]. The main mechanisms contributing to primary recovery and the resulting performances are strongly dependent on characteristics of a reservoir and flowing fluids [5]. Thus, considering the variation of reservoir rock, fluid properties, and heterogeneities, the recovery factor after primary stage varies from 20% and 40%, with an average around 34% [6].

After reaching primary residual oil saturation, the declination of production rates, as well as reservoir pressure, requires secondary recovery methods, such as water (or gas) injection to maintain the production performance above the beneficial level.

The secondary and tertiary stages of production can be implemented by two sub-categories: Improved Oil Recovery (IOR) and Enhanced Oil Recovery (EOR) respectively. Improved oil recovery methods mostly refer to new drilling, gas lifting, and well technologies. It may also include better reservoir management that was initially introduced in the late 1980s as an alternative to EOR methods due to oil price reduction. However, sometimes the definition of IOR methods is expanded to primary and also enhanced oil recovery methods [7].

Enhanced oil recovery (EOR) involves the introduction of a fluid into an oil reservoir that increases oil recovery. Since proposing the earliest EOR processes in the 1970s, the EOR projects have been strongly affected by crude oil price fluctuation [3]. The fundamental factors in choosing the proper EOR technique for a reservoir are the viscosity (or API) of the oil in place and formation characteristics. Miscible gas injection [8], water alternating gas (WAG) injection [9], polymer flooding [10, 11] and the use of surfactants [12] processes are frequently suggested for higher API grades. However, the heavier oils require steam injection and air injection, which leads to additional in-situ reactions, resulting in decreased viscosity by heat generation or molecular upgrading [13].

Normally, to pressurize and furthermore displace the medium to light residual oil, once the production rates decline during primary recovery stage, a water (sometimes gas) scenario is employed in reservoir production. Water availability, viscosity, low operating, and capital expenditures are the main reasons along with the relatively simple facilities' requirements to choose water for displacing light to medium gravity oil. Waterflooding is usually implemented in well pairs (offshore) and/or different patterns as shown in Figure 1-1. Economic and aerial

sweep efficiency are the key factors for selecting a waterflooding well pattern and operating conditions. Under ideal fluid and rock properties and the current injection scenarios, waterflooding performance ranges from 10% to 30% of the original oil in place (OOIP) [3].

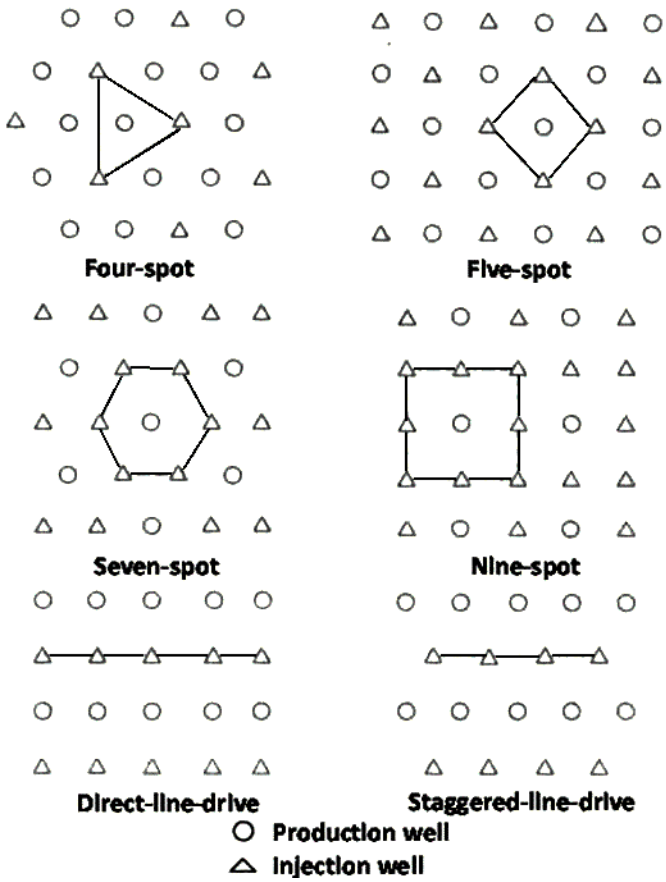

Figure 1-1. Popular regular waterflooding well arrangement [14].

The alternative step for water flooding in some cases is gas injection to maintain reservoir pressure and production quality.

A recent survey on field implementation of water (and gas) injection projects as a secondary recovery in the United States has shown lower oil recovery efficiencies for gas injection. However in some situations, including low permeability and a thin oil-bearing layer of some reservoirs where the solution-gas drive can be a key factor in displacing oil, gas injection is more realistic [15].

The ultimate RF attributed to water (or gas) flooding and employing further EOR methods can

be defined as the outcome of following function [16]:

$$RF = E_{ps} \times E_S \times E_D \times E_C \quad (1\text{-}1)$$

where, RF (Recovery Factor) is the standard volume of recovered oil per volume of oil initially in place (OIIP), E_{PS} (Microscopic Efficiency) is the fraction of displaced oil in contacted pores (microscopic scale) by the injected water (or gas), E_S (Macroscopic Efficiency) is the macroscopic proportion of the connected reservoir volume that is swept by the injected agent, E_D (Connected Volume) is the proportion of the total reservoir volume connected to wells and E_C (Economic Efficiency) is the physical and commercial restrictions on field life such as facilities life and reservoir energy.

The main purpose of EOR processes is to improve the microscopic efficiency (E_{PS}) and macroscopic efficiency (E_S). Therefore, characterizing and controlling the fluid, fluid-fluid, and fluid-rock parameters that influence these efficiencies are the key to improving microscopic and the macroscopic displacement of any EOR technique.

Microscopic displacement is governed by capillary and relative permeability effects. Based on the definition of capillary number, Equation 1-2, increasing of microscopic efficiency can be achieved by reducing the oil–water interfacial tension or increasing the viscose forces ($\upsilon\mu$) [17].

$$Ca = v\mu/\gamma \quad (1\text{-}2)$$

where Ca is the capillary number, υ is the interstitial velocity, μ is the fluid viscosity and γ is interfacial tension between wetting and nonwetting phases.

Formation heterogeneity or non-uniform distribution of permeability (or porosity and mineralogy i.e. wettability) can be the parameters that influence macroscopic recovery

performance (E_S). In most cases, this heterogeneity can lead to channeling in the stream of displacing fluid (water) [18]. Definition of mobility ratio M, Equation 3, can identify this effect as mobility of displacing fluid to displaced fluid.

$$M = (K_{rw}/\mu_{rw})/(K_{ro}/\mu_{Wro}) \quad (1\text{-}3)$$

where K_{rw}/μ_{rw} is mobility of water phase, the ratio of relative permeability of the formation (K_{rw}) to water viscosity (μ_{rw}), and K_{ro}/μ_{ro} is mobility of oil phase. Based on the mobility ratio, the viscosity and relative permeability are the dominant factors that affect the flow pattern in the reservoir. Therefore, a partial region of the formation that has a lower permeability to water phase will be bypassed in water flooding and decreases the macroscopic efficiency.

As mentioned above, the main purpose of most EOR processes is to boost microscopic and macroscopic (areal) sweep efficiencies by modifying the injectant fluid properties, the fluid-fluid properties, and fluid-rock properties. This may be achieved by injecting chemicals (such as surfactants or polymers) and by the injection of immiscible/miscible gases (carbon dioxide, natural gas, nitrogen or flue gases) to reduce IFT, alter wettability [19], plug the high permeability regions with polymers, and modify the viscosity of flowing phases.

Water alternative gas (WAG) looks to combine the advantages of gas injection coupled with water flooding to reduce a gas override and stabilize the flood front.

1.1.2 Micromodel Method for Enhanced Oil Recovery Screening and Challenges

Implementation of any new EOR method at the field scale requires some preliminary steps in advance to ensure the profitability and feasibility of the proposed scenario. For instance, a typical EOR project workflow is presented in Figure 1-2.

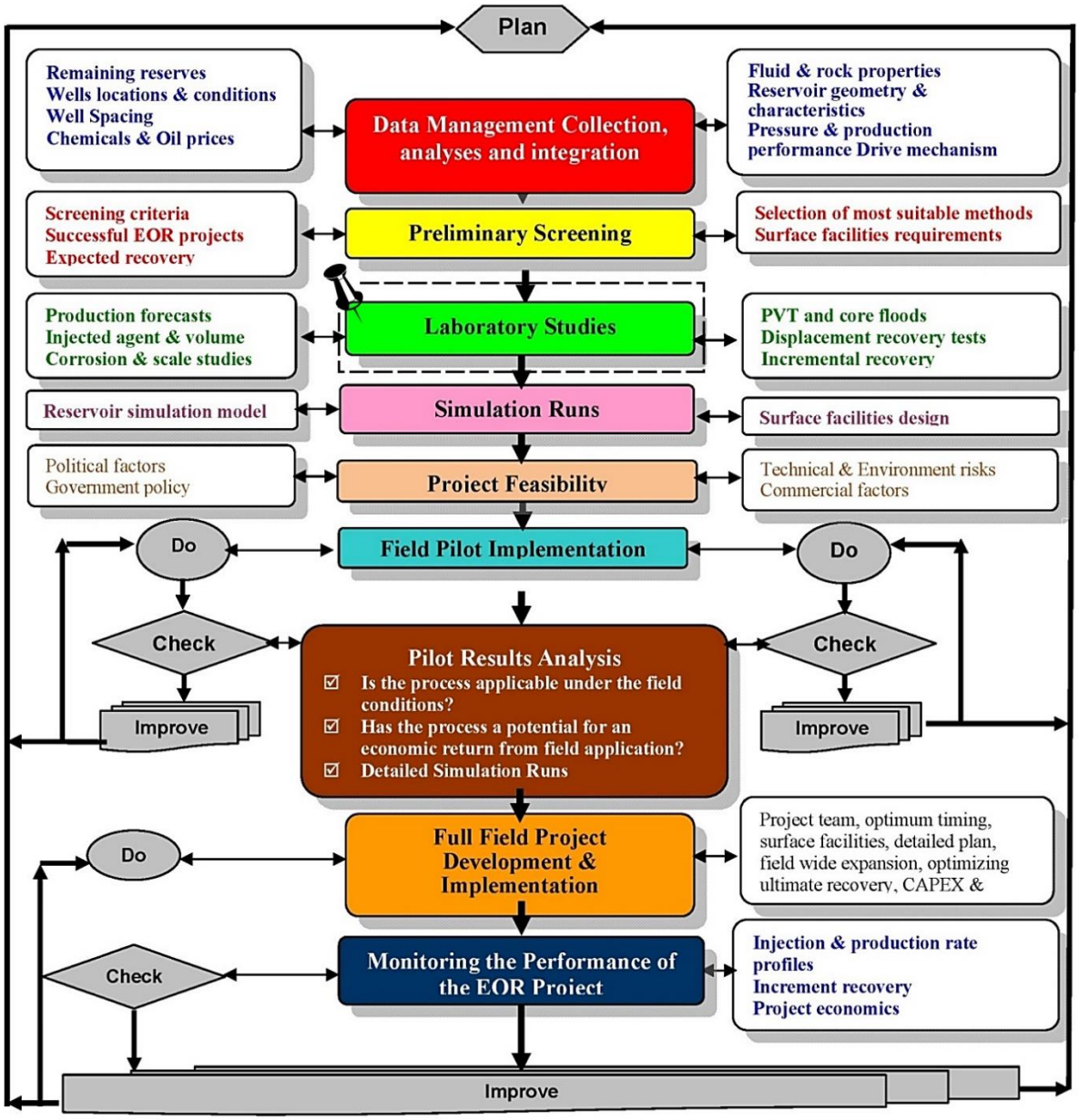

Figure 1-2. The general approach for implementation of an EOR project [20].

The initial step is providing a multidisciplinary data bank that includes geological, fluid/reservoir properties, and supplementary economic information. This integrated knowledge base is employed to analyze reservoir and oil characteristics in preliminary screening. Through this process, the proposed EOR methods are studied to identify the most suitable mechanism based on screening criteria, which are predetermined from prior EOR applications/projects, Table 1-1.

Table 1-1. Enhanced Oil Recovery Screening Terms [21]

Oil Properties				Reservoir Characteristics					
EOR Method	Gravity (°API)	Viscosity (cp)	Composition	Oil Saturation (% PV)	Formation Type	Net Thickness (ft)	Average Permeability (mD)	Depth (ft)	Temperature (°F)
Nitrogen and flue gas	>35↑ 48↑	< 0.4↓ 0.2↓	High percent of C1 to C7	>40↑ 75↑	Sandstone carbonate	Thin unless dipping	*NC	> 6,000	NC
Hydrocarbon	>23↑ 41↑	<3↓ 0.5↓	High percent of C2 to C7	>30↑ 80↑	Sandstone carbonate	Thin unless dipping	NC	> 4,000	NC
CO_2	>22↑ 36↑a	<10↓ 1.5↓	High percent of C5 to C12	>20↑ 55↑	Sandstone carbonate	Wide range	NC	> 2,500a	NC
Immiscible gases	>12	< 600	NC	>35↑ 70↑	NC	NC if good vertical permeability	NC	> 1,800	NC
Micellar/ Polymer and Alkaline Flooding	>20↑ 35↑	<35↓ 13↓	Light, intermediate	>35↑ 53↑	Sandstone preferred	NC	>10↑ 450↑	> 9,000↓ 3,250	> 200↓ 80
Polymer Flooding	>15	< 150, > 10	NC	>50↑ 80↑	Sandstone preferred	NC	>10↑ 800↑	< 9,000	> 200↓ 40
Combustion	>10↑ 16	< 5,000 - 1,200	Some asphaltic components	>50↑ 72↑	High-porosity sand/ sandstone	>10	>50	<11,500↓ 3,500	> 100↑ 135
Steam	> 8 to 13.5>	< 200,000 - 4,700	NC	>40↑ 66↑	High-porosity sand/ sandstone	>20	>200↑ 2,540↑	< 4,500↓ 1,500	NC

*NC: Not Critical

Following the results of the preliminary screening study, complementary laboratory research should be conducted to evaluate the performance of nominated recovery method. These laboratory studies can be broken down into various sub-categories. For instance, measuring physical/chemical properties of injected agents, running the PVT test for present reservoir fluids [22] and determining of relative permeability/wettability alteration [23-26]. Analyzing the predictable corrosion problems to the surface equipment [27] and performing the displacement tests in micromodels [28–31] or cores to simulate the effective factors' interaction during EOR process [32, 33] are some other advanced experimental studies.

The ongoing microscale interaction between influencing factors such as interfacial tension/forces, mass transfer, and gas solubility as well as injection rate and pore gas scale characterizations (i.e. pore size distribution, coordinate number and pore-throat aspect ratio) are the main concepts that dictate the performance of the involved larger-scale processes in oil production.

The increasing number of studies simulating the pore-scale interactions in the reservoir through microfluidic devices caused a significant popularity for micromodels [34] in oil and gas research areas. Since fabricating the earliest prototypes [35], the implementation of this methodology has provided better knowledge of a wide range of complex phenomena related to oil extraction. For instance, monitoring of wettability alteration [36], particle generation [37], miscible displacement in pore networks [38], screening of foam generation in emulsifiers/surfactants injection [39], and steam diffusion in heavy oil phases [28].

The EOR screening experiments in micromodel aimed to visualize and investigate various phenomena. There is a broad range of chemical/mechanical challenges that exist through the implementation of micromodel methods in this area, such as operating pressure limit, model transparency, and acid resistivity. Consequently, fabrication methods have been studied extensively [40] to address structural restrictions of micromodels. The prototyping procedures for micromodels can be categorized as follows: the Hele–Shaw and glass-bead models [41], optical lithography [42], etching [43], stereolithography [44] and soft lithography [45].

Depending on the etchant agent, chemical or plasma, the etching method can be called wet or dry etching. The main components in wet etching are the etchant, which is a hydrofluoric-base acid solution, and the silicon based substrate [46–48]. Following this method, the glass or the silicon-based surface (such as silicon wafer and quartz) is etched, and the masked areas with an acid resistant layer (such as photoresist or/and metal layer) remain unchanged. The width of

the created channel is controlled by the size of voids in the originally designed pattern, and it is usually less than 1 mm. The desired microchannel depth depends on the soaking time in hydrofluoric acid solution and etching speed, which is depending on acid's concentration (1 μm/min approximately).

The wet etching method, following the projecting the network mask on acid-resistant layer, has three basic steps: (i) transporting of the etchant to the surface silicon substrate; (ii) reaction between the etchant and the silicon substrate; and (iii) transport of the byproducts from the reacted surface [49]. The chemical reaction is summarized as follows:

$$SiO_2 + 6HF \xrightarrow{\text{yields}} H_2SiF_6 + 2H_2O \qquad (1\text{-}4)$$

There are a great number of publications on employing wet etching to fabricate micromodels that present different applications of this method and address the associated challenges. For instance, the round shape of cross section [50] is the result of isotropic penetration of acid in all directions during etching (Figure 1-3). This sloped pore wall can lead to optical refraction in phase boundaries, which is the major source of error in digital calculation, Figure 1-4. The presence of chemical impurities in the silicon substrate and/or an etching solution that is not optimized can cause some roughness at the channel surface that affects wettability and capillary forces [51].

The next complementary component in micromodel studies is the visualization of ongoing experiments and related features in the model. These features include the grain/pore size distribution in the pattern of the fabricated micromodel both before and after of model bonding step. This step includes some challenges such as choosing the proper recording system and designing the required algorithm to process/analyze the digital data that is sensed by a camera (sensor).

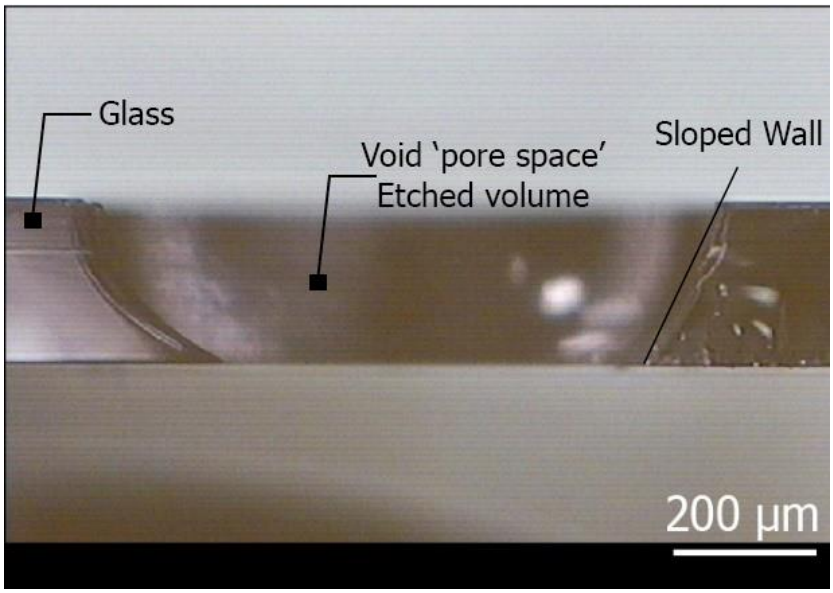

Figure 1-3. Cross-section view of the channel etched through glass [50].

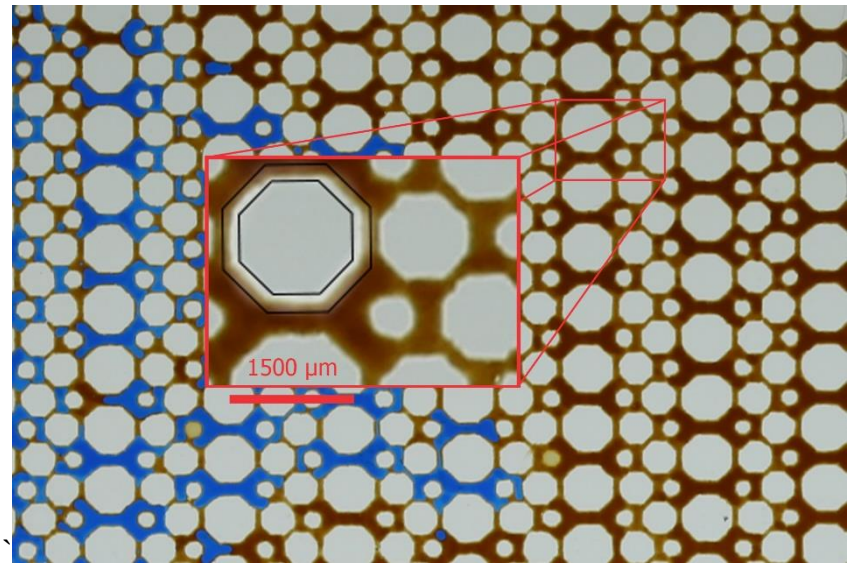

Figure 1-4. Refraction effect of the sloped wall in the oil-glass boundary.

In oil and gas research projects, the main focus in visualization of two (or three)-phase flow experiments is qualification or quantification of the attributed variables of interest, such as saturation and interfacial parameters [52]. The visualization process as shown in Figure 1-5 can be categorized as follow: microscope–camera [53], volumetric imaging [54] and direct camera visualization [55].

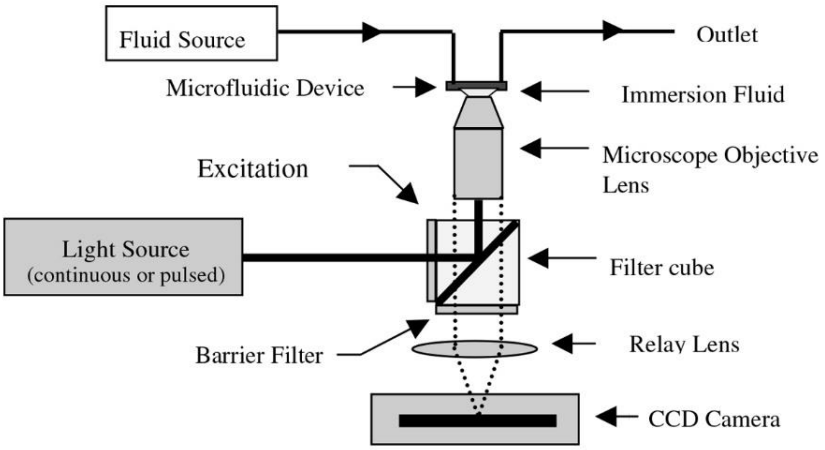

(a) Schematic microscope–camera [53].

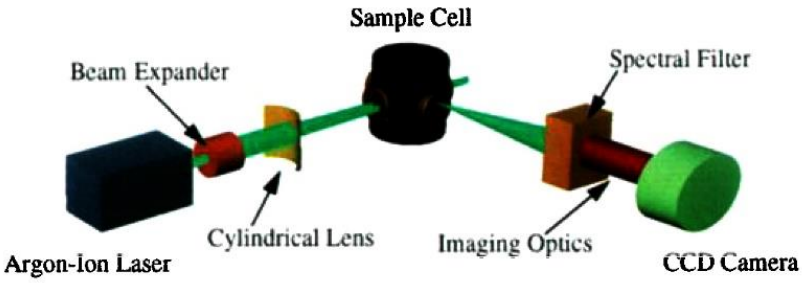

(b) The experimental setup for volumetric imaging [54].

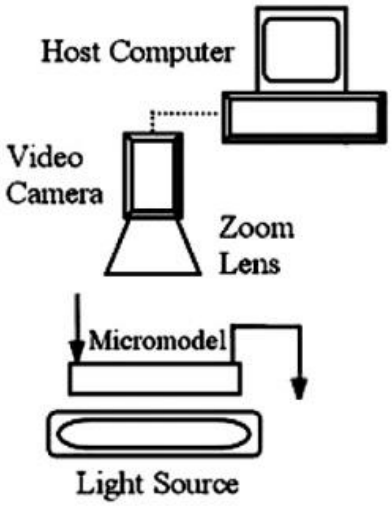

(c) Direct camera visualization setup [55].

Figure 1-5. The available visualization system for low-pressure micromodel experiments.

Based on the suitability and limitations of each visualization method, micromodel studies use an appropriate setup to gain a desirable resolution in visual acquisition of flowing fluid

configurations. Direct camera visualization, is a relatively economical approach in comparison to other visualization systems. Despite the lower resolution, the direct camera option has more flexibility in moving the sensor (camera) without causing any disturbance in the model. More importantly, the direct camera setup can capture high-speed effects happening in micromodel [40]. This feature is vital in micromodel studies that mostly investigate dynamic oil and water interactions in pore size. A typical schematic of a direct camera visualization system and other model injection components have been presented in Figure 1-6.

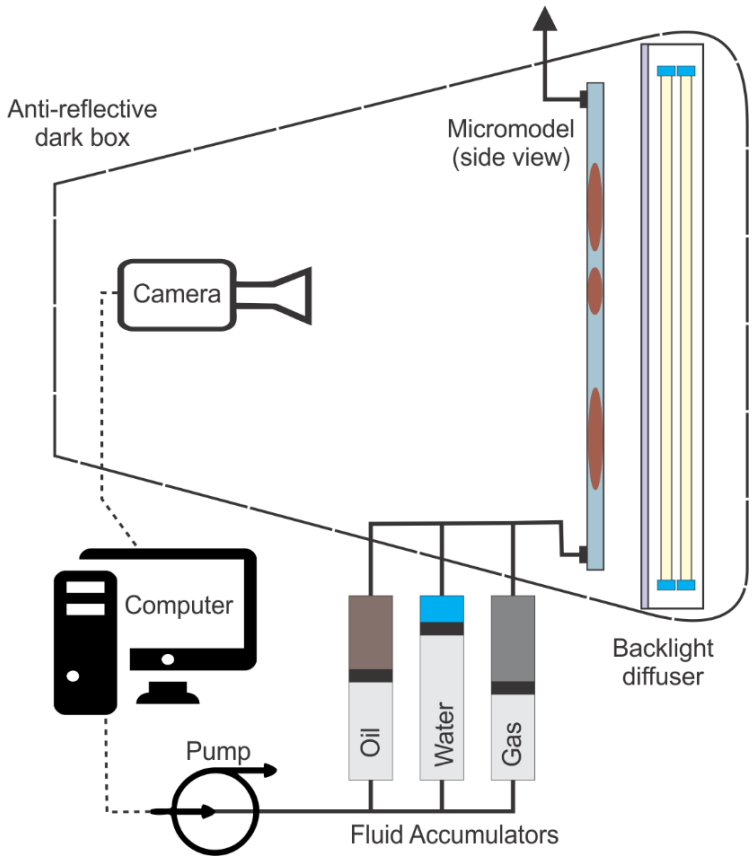

Figure 1-6. Schematic low-pressure micromodel visualization setup

Similar to other scientific and industrial fields in the last decade [56, 57], digital image processing and analysis has an essential role in the completion of visualization tasks to interpret the visual information understudying conditions.

Recent progress in equipment to capture higher resolution with faster frame rates, along with

the latest innovations in image-based programming languages, have extended digital image processing applications to multidisciplinary research areas [58]. This increased engagement of image processing with various research areas has led to newly established modules and improvement in compatibility.

The existing software that provides platforms to process/analyze image files have two categories:

Programming-based software: The software that contains relevant toolboxes and uses a particular language to develop an in-house code. Almost all languages offer a vision module. However, some platforms such as C++ has a lower language level, which requires an extensive professional knowledge to operate. New visual languages are the better option for a non-specialist programmer who needs to develop an image-based code. LabVIEW is one of the most advanced samples for visual programming.

Commercial Software: The available user interfaces in the market that offer pre-developed functions and image transformation tools are mostly utilized for commercial purposes, such as photography. Therefore, the image analysis software for scientific purposes are limited regarding capability and availability. Fiji [59] (also called ImageJ) is a popular software in this category, which has been widely used originally in the biological and then another field of studies that require visual quantification.

Laboratory Virtual Instrument Engineering Workbench (LabVIEW) is a system design platform and development environment for a visual programming language from National Instruments (NI), USA. Originally designed for simple laboratory automation, it has advanced to be known as a graphical programming language. LabVIEW is popular because it can simplify complex functions such as capturing high-quality images in databases and accomplishing large post-processing tasks more easily than other available languages [60]. In

addition to the simplifying of computational aspects, there are other associated applications in LabVIEW for processing micromodel experiments. For instance, the potential to synchronize the capturing of visual information with the recording of other experimental data types, such as pressure and temperature, can provide real-time data acquisition [61]. Also, the dedicated Vision Assistant interface in LabVIEW simulates a virtual laboratory for programmers to test their image processing algorithm parts before implementation into final VI.

The visual features and distinct fluid phases in the captured images during a typical oil-water-gas displacement test, need advanced image-based functions to fulfill enhanced oil recovery linked measurement requirements.

The commonly measured parameter in micromodel is the saturation of flowing fluids as a function of pore volume injected [62]. Swelling factor [63], interfacial area per volume (IAV) [52] and particle velocity [64] are the other factors that Image processing algorithms extract from raw micromodel images. The associated errors with image-based quantification in micromodel studies, due to equipment and calculation methodology sources, are not addressed sufficiently in previous enhanced oil recovery visualization works. However, the error evaluation methods are well developed through other multidisciplinary research projects that shed light on the linked errors to image processing/interpretation techniques. The biological investigations and fluid displacement studies need a similar algorithm, while the optical features and object geometries of understudy samples are equivalent [65, 66]. Therefore, the common error assessment strategies in other visualization projects, such as misclassification error (ME) and segmentation uncertainty (UT) [67], can provide a measure to adjust the controlling parameters of used functions in the procedure of micromodel digital image analysis.

1.2 Purpose of Study

The main goal of this research is to improve two essential steps involved in the micromodel study method that is employed to screen enhanced oil recovery mechanisms: i) Micromodel fabrication and ii) Image processing.

First, one of the popular fabrication methods for glass micromodels, wet etching, is partially modified in such a way that the previous masking approaches such as lithography is replaced with a new laser engraving technique. This modification aims to simplify the fabrication technical difficulty by avoiding the necessity of clean room that was required for coating the photoresist. Also, the costs and the hazardous concerns related to chemical handling is reduced as result of replacing former masking procedure that consequently allows the researchers to produce a model with more complexity in the network's pattern with a larger size.

The more significant improvement that is proposed in this research is the application of an advanced programming platform, such as LabVIEW, to proceed complex image processing/analysis algorithms for a large number of high-quality images from micromodel visualization experiments. The benefits of this application can be highlighted when the visual data is captured dynamically and then require a further extensive interpretation.

Accomplishing these two milestones has some challenges based on similar works and literature. This research tries to propose a comprehensive methodology to address those challenges. Therefore, the main objectives of this research can be listed as follows:

- Simplify the masking step in wet etching method to fabricate glass micromodels,
- Optimize the laser engraving operational parameters to improve the quality of the etched microchannels,
- Test the new fabricated micromodel at experimental conditions to evaluate the proposed

alternative method,

- Design and develop an effective image analysis algorithm based on the essential terms in the micromodel study of enhanced oil recovery using the dedicated vision module in LabVIEW interface,
- Define a specific evaluation procedure to estimate the associated micromodel image analysis errors, and
- Employ the defined assessment process to compare the performance of available image functions in LabVIEW and find the one with the lowest deviation from true values that is calculated by non-visual methods (volumetric calculation).

1.3 Thesis Structure

The following chapters of this thesis are organized based on Memorial University's guidelines for thesis and report formatting. The second chapter will present the drafted paper on a quick, low-cost method to fabricate large glass micromodel networks. This article introduces an alternative laser-engraving technique to modify common masking approaches in wet etching method for glass micromodel fabrication, using a CO_2 laser machine. After reviewing the involved steps in wet etching, a new laser masking method is introduced and combined with recent advances in wet etching fabrication to make a sample prototype. The final product is tested under actual experimental conditions to evaluate the proposed process.

The third chapter presents the prepared article on advanced image processing for micromodel flow experiments: an application using LabVIEW. This paper aims to develop an efficient algorithm to process and then analyze the raw images that are acquired during a micromodel visualization test. Next, the designed algorithm is coded in LabVIEW platform that offers a graphical user interface and an advanced vision module to programmers. Finally, a proper evaluation is adopted from previous visualization references to optimize the controlling

parameters in analysis process based on our application, which is to quantify the captured images from microfluidic experiments.

The last chapter of this thesis is devoted to summarizing the research findings along with obtained conclusions. A corresponding section is added to suggest some research directions for future recommendations.

CHAPTER 2
A QUICK, LOW-COST METHOD TO FABRICATE LARGE GLASS MICROMODEL NETWORKS

2.1 Abstract

Micromodels have provided a wide range of opportunities for research areas that investigate the behavior of fluids in microscale. The variety of micromodel applications in chemical and biological studies has motivated to develop new methods and use different materials to overcome fabrication challenges and meet different experimental purposes. This paper aims to modify and combine the recent advances in chemical (wet) etching method to fabricate a glass micromodel and provide a low-cost, efficient alternative procedure. The general steps of this processes are masking, etching, and bonding. First, the common masking step (projecting the designed pattern on the acid-resistant layer) in this work is simplified by engraving the mirror plates with a CO_2 laser. This new technique skips the photoresist layer deposition and then UV lithography by using pre-coated soda lime glasses (mirror). Also, the variety of mirror products and flexible functionality of laser machines make it possible to create larger size models with any desirable flow pattern. The general composition of solution used in the etching step and the operational conditions of thermal bonding are modified based on recent investigations in literature to enhance the mechanical strength of the micromodel. Finally, the fabricated model is applied in a two-phase flow visualization study to examine the practical features under experimental conditions.

2.2 Introduction

Since the earliest prototypes were introduced [35], micromodels have provided fluid flow visualization through microchannel networks. There are a growing number of multidisciplinary

studies that use microfluidic devices to understand ongoing mechanisms in more detail. This objective requires further developments and modifications of micromodel types based on the underlying process conditions. Accordingly, model fabrication methods and alternative materials have been investigated extensively [40]. The prototyping procedures for micromdels that are widely mentioned in the literature can be categorized as follows: the Hele–Shaw and glass-bead models [41], optical lithography [42], etching [43], stereo lithography [44], and soft lithography [45].

Depending on the etchant agent, chemical or plasma, the etching method can be called wet or dry etching. The expanded facility that is required for (stereo) lithography and dry etching along with the limited application range of these methods have caused a relative popularity for the wet etching technique.

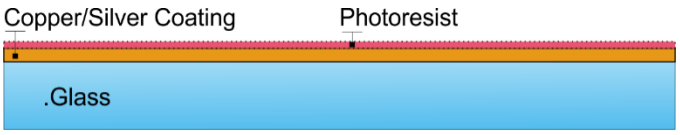

(a) – Photoresist coating on glass surface with (or without) metal layer

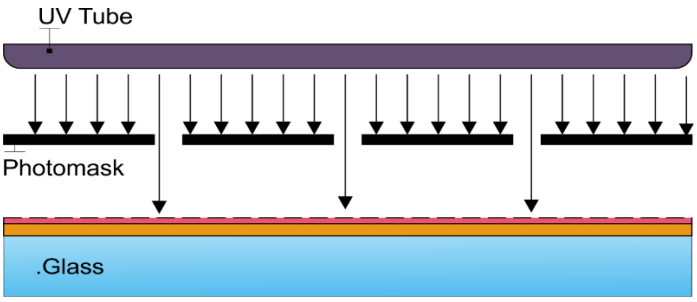

(b) – UV light radiation through the photomask

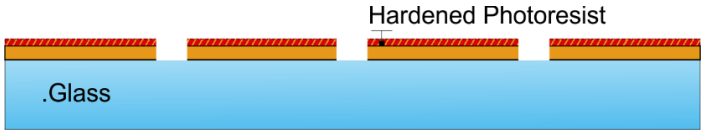

(c) – Washing developed photoresist mask (and the metal layer)

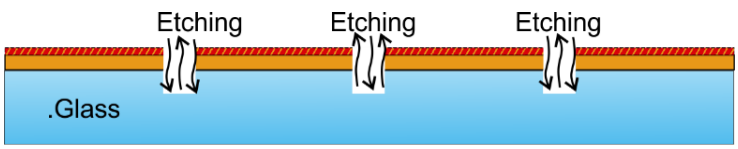

(d) – Wet etching in the HF solution

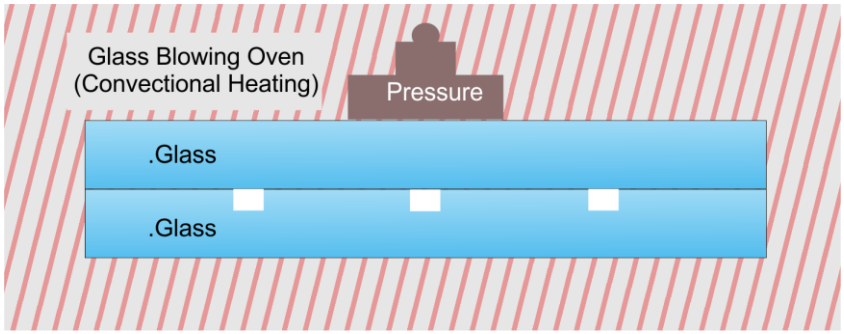

(e) – Thermal bonding with assisting static pressure

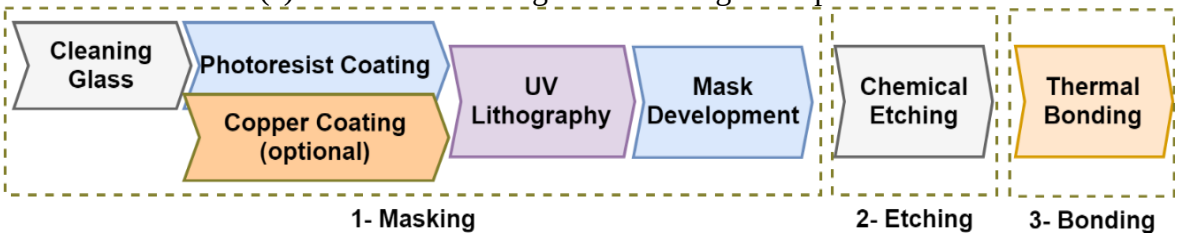

(f) – Overall chemical etching procedure

Figure 2-1. Schematic steps of wet etching fabrication.

As presented in Figure 2-1f, the overall mentioned sequences in previous works for wet etching fabrication are *masking*, *etching*, and *bonding*. Throughout masking, a glass plate with (or without) a primary metal coating is initially covered by a thin layer of photoresist in a spin coater machine, Figure 2-1a. Next, the desired network pattern is printed on a transparent material (photomask), and then the model is exposed to ultraviolet (UV) light through the photomask in a mask aligner, Figure 2-1b. Subsequently, exposed plate is immersed in the developer solution. During photoresist development, the areas of the photoresist exposed to UV become soluble in the developer and the unexposed areas remain insoluble. Finally, the soluble flow channels are washed away by distilled water to form the network mask on the glass. In the case of photoresist-metal combined coating, a diluted nitric acid solution is then employed to remove the remaining metal layer in flow channels, Figure 2-1c. Because of the required precision in photoresist coating and lithography, the concluding quality of fabrication process strongly depends on the choice of coating materials as well as the precession of masking procedure.

The etching step includes an acid solution as a chemical agent that dissolves the silicon-based

materials such as glass, quartz, or silicon wafers [46] and creates flow channels (< 1 mm) in unmasked areas, Figure 2-1d**.** The mechanism occurring in this process is a simplification of silicon oxide dissolution into hydrofluoric acid. Equation 1 describes the overall etching reaction below:

$$SiO_2 + 6HF \xrightarrow{\text{yields}} H_2SiF_6 + 2H_2O \qquad (2\text{-}1)$$

As a parallel reaction with equation 1, the existing oxide components such as CaO, Al_2O_3 and MgO (impurities) in the glass composition react with acid and yield insoluble products in the HF solution [49]. As reported in the literature, these insoluble products create an undesirable film on the etching surface, which is the main factor in challenges in the chemical etching process such as etching rate reduction over time and unwanted roughness formation on the surface [68].

The final part of this procedure is to bond the etched glass plate with another identical flat plate, Figure 2-1e. Based on various applications for the micromodel, several bonding techniques such as anodic, adhesive, eutectic and thermal bonding have been developed [69]. Despite the complexity of thermal bonding, this method is a well-known process that does not require any supplementary material to seal micromodel plates which may cause additional costs (eutectic bonding) or operational challenges (adhesive bonding). Accordingly, recent studies [70, 71] on thermal bonding mostly focus on modification of the fusing process and introduction of chemical pre-treatments to strengthen the attachment forces between glass plates.

As a major part of this paper, the conventional lithography masking is replaced by CO_2 laser engraving. With the help of this new method, the hazards of exposing to UV light and the associated expenses with photoresist utilization, such as the coating spiner and clean room facilities are reduced significantly. Also, and most importantly, laser engraving is an efficient

and fast process without any pattern size limitation which can be used to fabricate larger models for different purposes.

Additionally, the second part of this work aims to adopt the current advances from conducted researches on etching buffer composition [72] along with a thermal assisted direct bonding technique (TADB) [70, 71, 73, 74] to overcome the challenges mentioned in etching and bonding steps.

Following the thermal assisted direct bonding technique patented and developed by Chen [70], a surface treatment is performed on the glass before fusing that is a prominent adjustment that eliminates contaminating factors in thermal bonding [75, 76].

2.3 Material and Methods

2.3.1 Masking

The masking procedure is accomplished in two phases. First, the desired flow network is designed using CorelDraw X7 at a magnification of 1:1 and resolution of 600 dpi. Second, the pattern is engraved onto the backside of the mirror with a CO_2 laser engraving machine [Trotec SP300, USA]. The generated geometry for the micromodel can be homogeneous, which are designed to investigate particular transport phenomena in porous media, or non-homogeneous, which means that pore features adopted from a thin section image of real rocks. Two samples of homogeneous and non-homogeneous patterns are shown in Figure 2-2. As shown in this figure, the geometrical features of designed grains and the overall size of the micromodel are flexible in this new masking method. However, these two important factors in the conventional UV/photoresist masking procedure are relatively limited by the technical constraints and required facilities. For instance, the clean room that is necessary to avoid possible contaminations during the coating process and the device restriction in other fabrication methods (plasma etching and UV lithography) for masking larger models.

The smallest possible sizes of pores and grains in the original digital pattern are restricted by the machine's laser beam size (pore width > 150 μm) and masking layer bonding stability in the etching solution (grain dimensions > 2*2 mm).

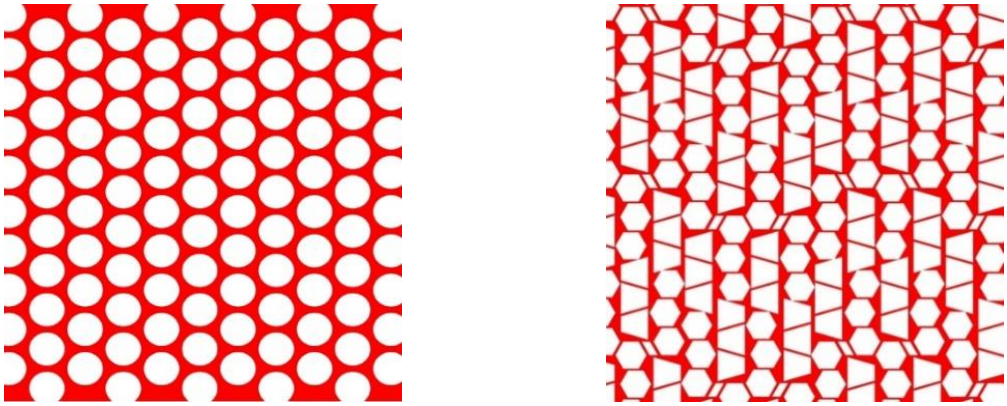

(a) (b)

Figure 2-2. - Two samples of network patterns; (a) homogeneous, (b) non-homogeneous.

As presented in Figure 2-3**,** during the engraving process the copper-silver layer must be removed without affecting the surface of the glass. Any microfracture generated by the laser on the glass (Figure 2-4a) surface has a potential for further failures in model construction (Figure 2-4b).

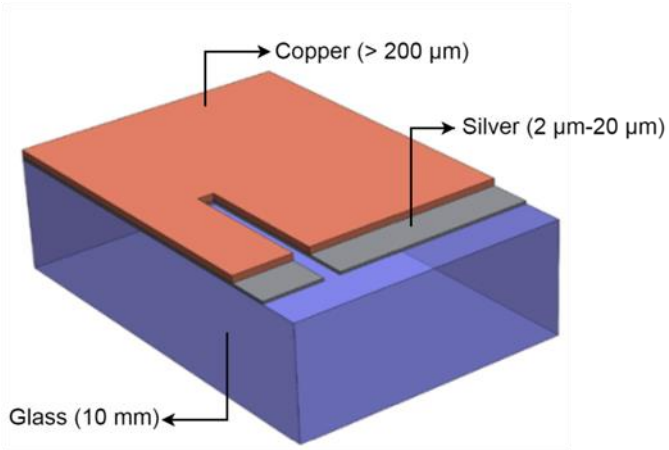

(a)

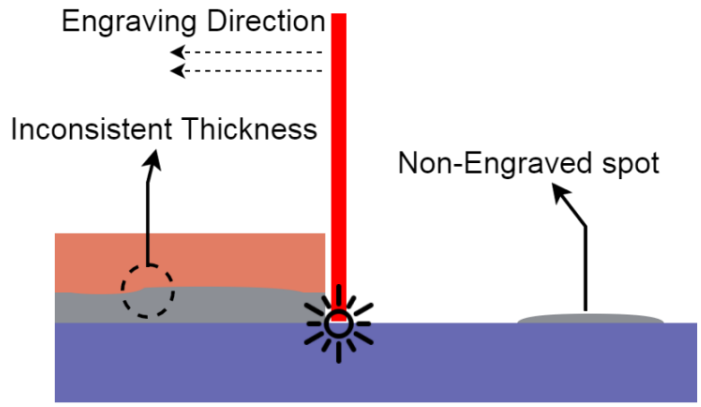

(b)

Figure 2-3. CO2 laser engraving of mirror's back (copper-silver) layer; (a) 3D view, (b) side view.

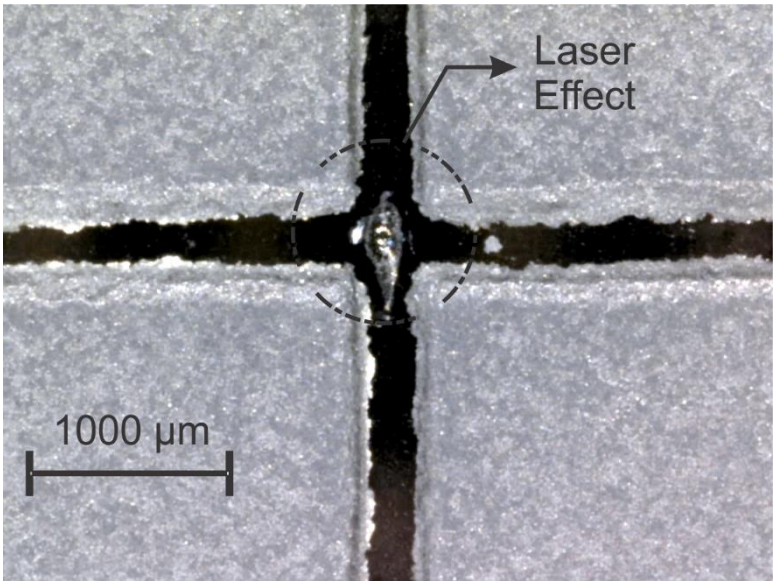

(a)

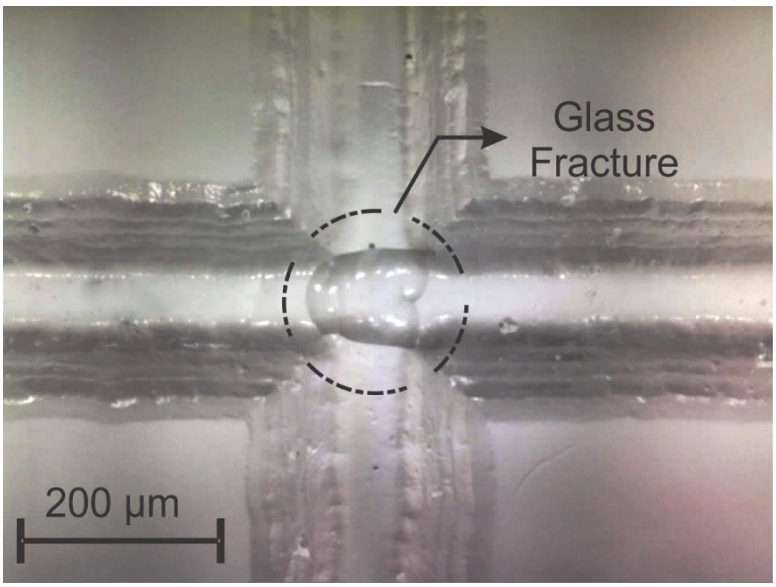

(b)

Figure 2-4. The side effect of laser engraving on a glass surface; (a) before etching, (b) after etching.

Therefore, a trial and error experiment method was performed to examine the effects of CO2 laser parameters, including engraving speed S and fractional power Pf, on the mirror plates. In this part, the fractional power was increased stepwise from 10 to 20 W while for each step the speed was varied from 5 to 25 m/min and other controlling parameters such as working mode, masking test-pattern (Figure 2-5a) and laser frequency were kept constant. After repeating this procedure for each power/speed test condition, a microscopical inspection was conducted to evaluate resulting surface quality by counting the number of engraving failures in test-pattern's channel cross nodes (8*8 = 64 total nodes). As shown in Figure 2-5, the failure in the laser engraving can be either the microfractures caused by excess laser flux (Figure 2-5b) or the non-engraved spots due to insufficient laser flux (Figure 2-5c).

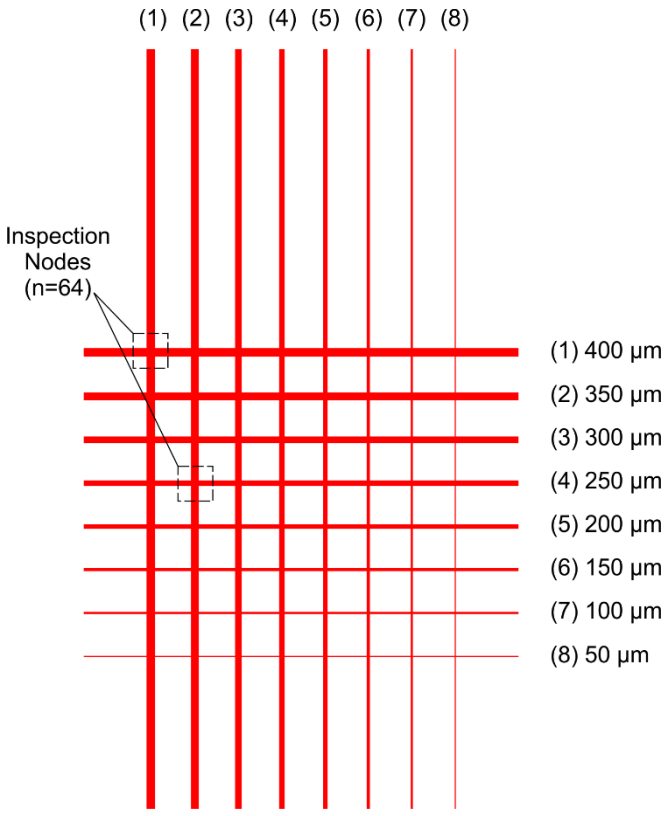

(a)

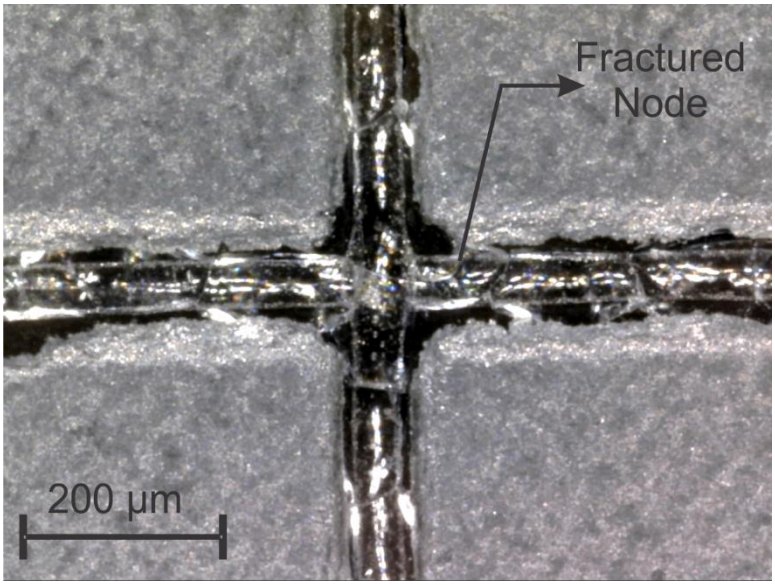

(b)

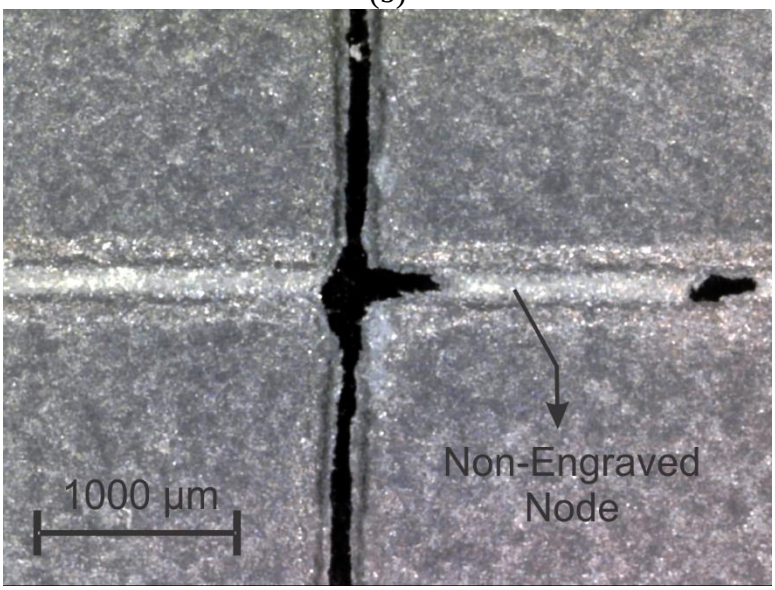

(c)

Figure 2-5. The illustration of trial and error tests for optimizing masking step; (a) test-pattern design, (b) effect of laser excess power and (c) effect of insufficient laser power.

Finally, based on the presented failure probabilities distribution plot (using MATLAB) for different power/speed test conditions (Figure 2-6), a set of optimized settings which showed the minimum failure probability is determined and presented in Table 2-1.

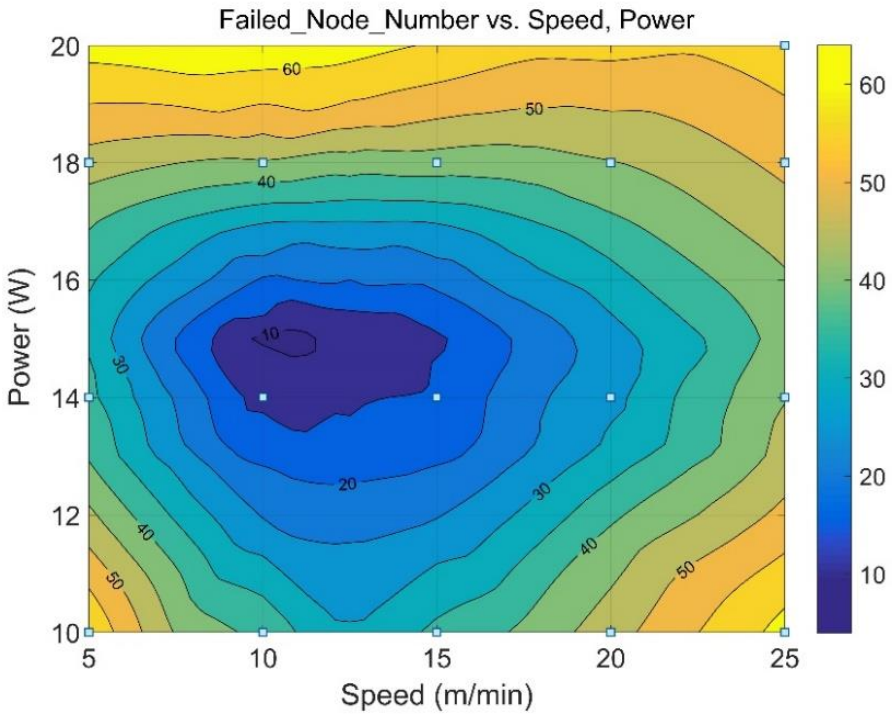

Figure 2-6. The linear regression of failure probability in laser masking method (R-square = 0.917)

Table 2-1. Laser machine optimized engraving settings

Parameter	**Mode**	**Power P_f**	**Speed S**	**Frequency**
Value	Engraving	15 - 16 W	10 - 12 m/min	1000 Hz

Due to the different thicknesses of the metal layer of mirror plates (especially for large size mirror plates) some non-engraved spots might remain and block narrow channels, Figure 2-3b. Therefore, the model is exposed to a solution of 5% nitric acid for 5 seconds and then is rinsed with tap water. This cycle is repeated and microscopically examined to ensure that the glass is completely exposed as the micromodel pattern has no copper-silver left on the desired pore regions. Finally, the masked model is rinsed with a solution of 1:1 distilled water and methanol and then baked in an oven at 120^{o} C for 10 minutes to maximize water evaporation [77].

2.3.2 Wet-Etching

The hydrofluoric-based wet-etching method is a low-cost and fast approach compared to dry etching methods [46]. The solution used in this research is adopted from an experimental optimization done by Marten [72]. Through his research, it was shown that the smoothness of

etched channel walls in a soda lime substrate is enhanced by the addition of HCl acid to the conventional buffered HF fluid that is frequently used in wet etching of a glass surface, as demonstrated in the SEM image of etched glass samples, Figure 2-7.

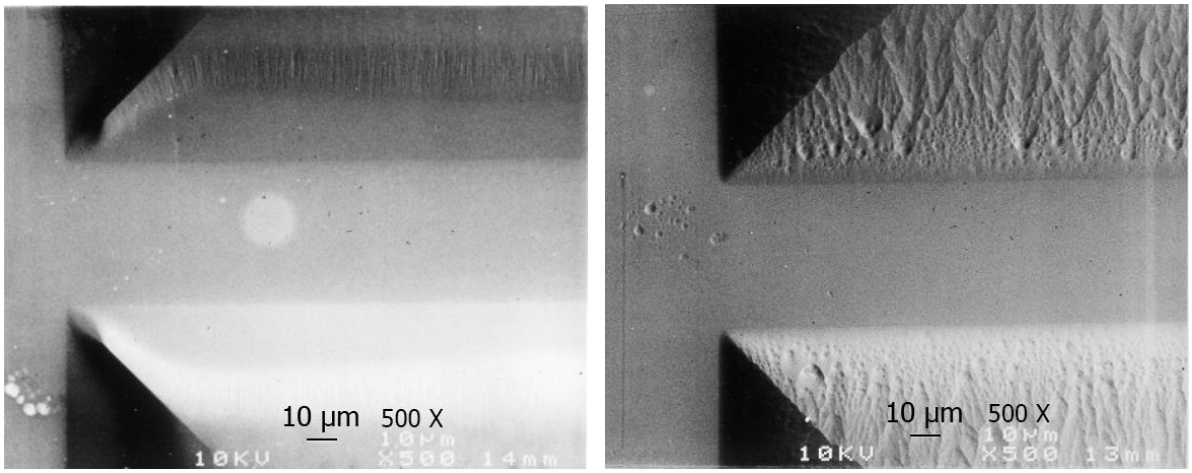

(a) (b)

Figure 2-7. The effect of HCl addition to etching buffer; (a) with HCl, (b) without HCl [72]

Following this procedure, initially, the other side of the mirror is covered with an (approximately 500 µm) acid-resistant adhesive layer [3M, USA] to prevent the glass surface from having any contact with the etchant buffer. Then, the etching is performed in a well-stirred aqueous mixture of 5% buffered HF (7:1 NH_4F (40%) - HF(50%)), and 9.25% concentrated HCl for 60 min under a fume hood. Due to the precipitation of insoluble components during the reaction, the glass plate was immersed face down in a standard etching plastic container and every 20 min the model was safely brought out and rinsed with distilled water. The resulting models were investigated in a scanning electron microscope (SEM) and are displayed in Figure 2-8. The measured properties of fabricated microchannels are presented in Table 2-2.

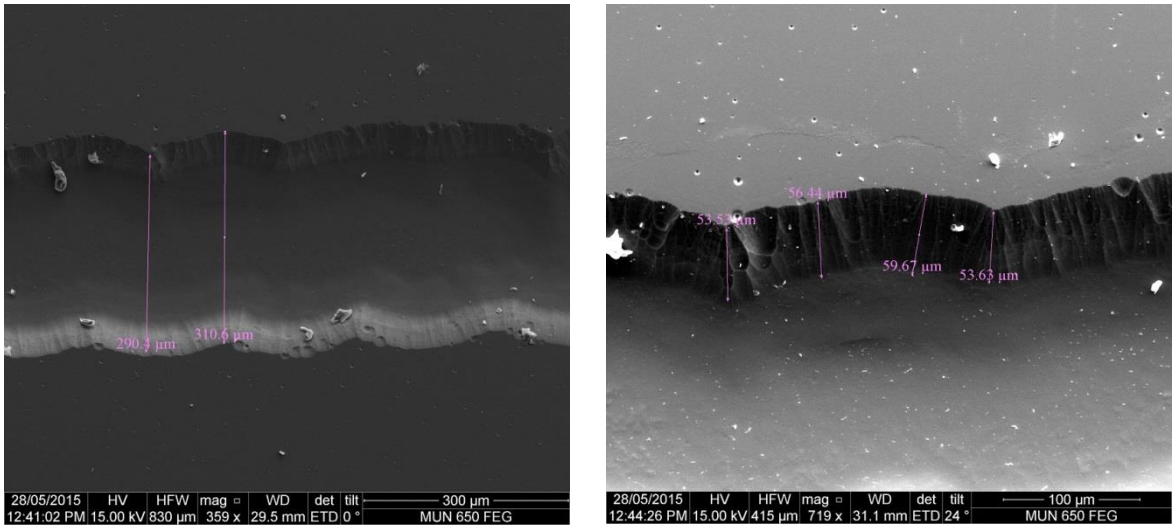

(a) (b)

Figure 2-8. The SEM images of etched channels; (a) top view, (b) tilted view

Table 2-2. Sample channel geometrical feature (after 60 min etching)

Feature	**Etching rate**	**Engraved Channel Width**	**Etched Channel Width**	**Etched Channel Depth**	**Channel Slope**
Value	1 µm/min	200 µm	280 – 300 µm	55 – 70 µm	24 - 28 ^{o}

2.3.3 Bonding

The bonding of an etched glass (also called structured) plate to another flat plate is the final step in micromodel fabrication. In this paper, a thermal assisted direct bonding technique (TADB) [70, 73, 74] is employed to seal the etched plates with another glass plate. This low-cost method comprises two subsequences; *i) Pre-cleaning* and *ii) Direct assisted thermal bonding* in a conventional furnace.

Initially, the unexposed portion of the mirror plates, which is not etched and is covered with a protective paint layer, is perfectly cleaned with a toluene-based paint cleaner [Recochem, Canada]. The model is then placed in 50% nitric acid solution [77] to remove any remaining metal coating from the glass surface.

Any dust/particles on the glass plate will prevent full bonding by reducing surface area contact. If this issue is extended to the large unbonded areas, the micromodel could fail under

experimental forces such as high flow rates and/or high pressure. Therefore, a cleaning solution has been employed to prevent this problem during bonding. The influence of the pre-cleaning solution, with variable compositions, on final bonding forces is studied by Chen [71]. As results showed, the higher bonding quality was achieved after employing the optimized cleaning solution (NH_4OH–H_2O_2–H_2O, 0.5:1:5 volume ratio) at 70^o C for 10 min and washing the model with DI-water. The particle removal efficiency of this treatment will decrease in a low concentration of NH_4OH, and a high concentration of NH_4OH will generate unsuitable roughness on the surface [78].

After cleaning, the next step is to bond the cleaned soda lime glasses thermally under external static pressure. Based on the optimized bonding condition of the glass substrate in conventional furnaces [Euclid Kilns CST-708F, USA] [74], the plates heated up by 5^o C/min and held at 610^o C for 240 min. All bonding is performed entirely under 28 KPa pressure generated by polished graphite plates as weights, Figure 2-9**.**

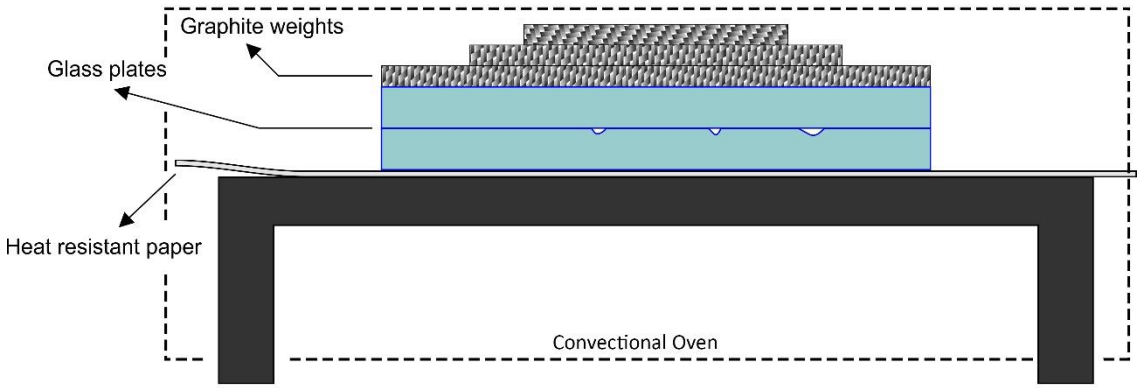

Figure 2-9. The glass plate fusing orientation.

The drilling of input and output holes in a soda lime model is a challenge due to the possible breakages or misaligned holes on both sides. Therefore, based on the method presented by available technical resources [79], two injection and drainage holes are drilled using a proper glass drill [North Jersey Diamond Core, USA].

2.4 Results

To evaluate the illustrated procedure in this study, two micromodels with the same network pattern (Figure 2-10). but with different margin sizes are fabricated and then tested through a multiphase flow experiment. In this experiment, a common combination of reservoir fluids (oil, water, and CO2) are injected under medium pressure, controlled flowrates (0.0001 - 0.01 ml/min) and ambient temperature to measure the absolute permeability of model. Next, the injection pressure is gradually (50 kPa/min) increased 500 kPa and held for 60 minutes. This process is repeated step by step until the breakage pressure is reached. The experimental measurements and the result of these pressure tests for two sample models (with different network margin sizes) are presented in Table 2-3. Furthermore, to compare the performance of the proposed fabrication method with other methods (UV lithography) two micromodel experiments utlized in the similar carbon-water-oil displacement are presented in Table 2-3**.**

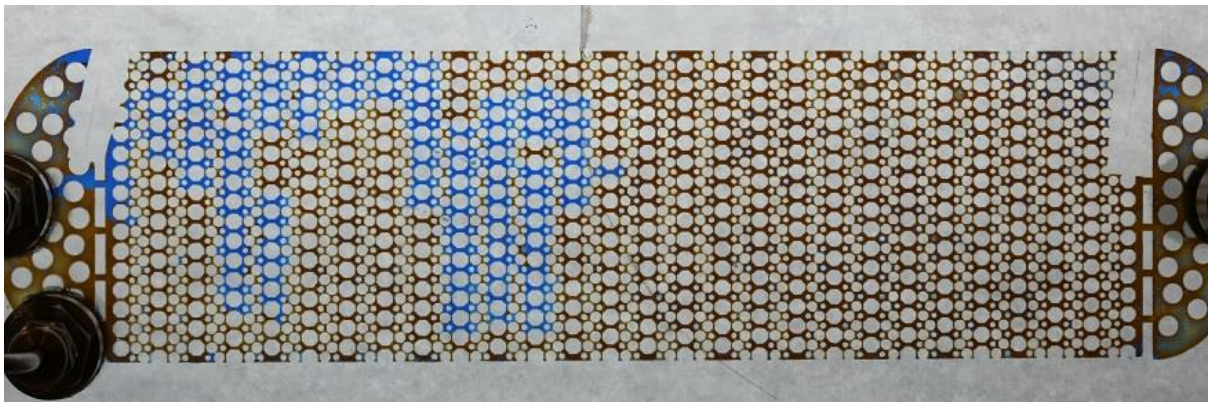

Figure 2-10. Sample soda lime glass micromodel

Table 2-3. Experimental information of fabricated micromodel.

Model Features				
Model Dimension	**Micromodel A**	**Micromodel B**	**Micromodel 1** [80]	**Micromodel 2** [81]
	120 x 300 mm	120 x 300 mm	30 x 60 mm	40 x 70 mm
Porous Media Dimension	80 x 260 mm	40 x 200 mm	6 x 38 mm	20 x 35 mm
Porosity	28.9 %	28.9 %	24.1 %	21.2 %
Channel Depth	75 µm	70 µm	35 µm	10 µm
Max Channel Width	300 µm	300 µm	300 µm	500 µm

. Experimental Condition				
Maximum Working Pressure	1500 - 2000 kPa	2000 - 3000 kPa	3500 kPa	2000 kPa
Breakage Pressure	4200 kPa	5800 kPa	NA	6000 kPa
Temperature	26° C	26° C	38° C	25° C
Flowrate	0.001 ml/min	0.001 ml/min	0.0016 ml/min	0.0001 ml/min

2.5 Conclusion

The preliminary evaluation shows that the produced model in this paper can be used for multiphase flow studies under slightly higher pressure than ambient pressure. This conclusion was confirmed by repeating this modified fabrication method and employing the constructed glass micromodels (with various margin size) into a set of multiphase displacement experiments as exemplified in Table 2-3. According to the model pressure tests, increasing the network margin size can elevate the pressure tolerance of model structure and it is required to be considered in micromodel design step. The required time and budget for new masking approach are convincingly reduced by substitution of involved steps in previous masking procedure (metal coating, photoresist spinning and UV exposure) with single laser engraving step. Another accountable advantage of this technique is avoiding the hazards associated with photoresist, UV light and developer solution. Additionally, the dedicated software in laser machines as well as flexibility of proposed masking method allows designing any pore network with larger network size than micromodels conventionally fabricated using UV lithography and complex geometry while the injection pressure can be maintained adequately as high as other micromodel studies (Table 2-3). These features have expanded the productivity of wet etching method which underlines the main purpose of this paper.

CHAPTER 3
ADVANCED IMAGE PROCESSING FOR MICROMODEL FLOW EXPERIMENTS: AN APPLICATION USING LABVIEW

3.1 Abstract

The study of multi-phase fluid flow in microfluidic devices provides an opportunity for researchers to observe fluid transport mechanisms and characterize influencing factors directly. The visual outcome of a micromodel experiment is the subject of further image processing/analysis studies that quantify the variables of interest such as fluid saturation and other morphological features. The application of image-based computational techniques offered by various programming languages allows us to quantify better results from micromodel experiments. In this paper, the viability of image processing functions available in LabVIEW is demonstrated by a sample image processing code. The performance of this custom algorithm is verified by comparison of extracted data from a carbonated water injection (CWI) micromodel experiment with estimated absolute values derived from volumetric material balance. Through this procedure, a collection of optimized settings for utilized functions in LabVIEW is found that shows a significant agreement with true values. In the last section, the implementation of the presented algorithm in the LabVIEW and a popular commercial software are compared to highlight the pros and cons.

3.2 Introduction

Micromodels have been extensively used for over 50 years to visualize the behavior of fluids in diverse research areas including chemical, biological, and physical research [40, 82]. The

Enhanced Oil Recovery (EOR) related research area is a popular field of application for micromodel experiments [34, 83]. These studies aim to improve the understanding of flow mechanisms and phase interactions between reservoir fluids that may contribute to increased oil recovery from hydrocarbon reservoirs [28]. This study uses digital images captured during a carbonated water injection experiment performed in a glass micromodel.

Carbonated water injection (CWI) is an immiscible flooding process where carbonated water is injected into the reservoir to increase oil recovery [84]. Potential recovery mechanisms that may assist in increasing oil production during the CWI process include oil swelling, oil/water interfacial (IFT) reduction and wettability alteration. These mechanisms are the focus of the visualization experiment. To analyze aspects of CWI micromodel experiments beyond the physical observation of pressure and temperature, digital image processing techniques are required to quantify key parameters such as fluid saturations, the size distribution of trapped oil bubbles and interface curvature. However, appropriate processing of the captured digital images from micromodel experiments has long been a source of complexity.

Digital image processing has played an ever-increasing role in different scientific and industrial fields in the last decade [56, 57]. Digital images are the direct conversion of visual information sensed by a camera (sensor) to a computer-readable data file, which can be processed later using available computational techniques. Recent advancements in digital equipment to capture higher resolution images, concurrent with further developments in image-based programming languages, have expanded digital image processing applications to multidisciplinary research areas [58]. This increased image processing engagement in research led the programming languages to establish new function collections (toolbox) and to improve their compatibility.

Laboratory Virtual Instrument Engineering Workbench (LabVIEW) is a system design platform and development environment for a visual programming language from National

Instruments (NI), USA. Originally designed for simple laboratory automation, it has advanced to be known as a graphical programming language. LabVIEW is popular because it can simplify complex functions such as capturing high-quality images in databases and accomplishing large post-processing tasks more easily than other available languages [60]. In addition to the simplifying of computational aspects, there are other associated applications in LabVIEW for processing micromodel experiments. For instance, the potential to synchronize the capturing of visual information with the recording of other experimental data types, such as pressure and temperature, can provide real-time data acquisition [61]. Also, the dedicated Vision Assistant interface in LabVIEW simulates a virtual laboratory for programmers to test their image processing algorithm parts before implementation into final code.

At first, this article presents an algorithm that consists of a relevant set of digital image processing and analyzing functions offered by IMAQ vision module of LabVIEW that aims to interpret visual data captured during multiphase fluid flow experiments in a micromodel. This section defines theoretical aspects of introduced LabVIEW code that prepare and then analyze the generated raw images from microfluidic devices. The preparation (*Initialization, Monochrome Plane Extraction* and *Non-Uniform Background Correction*) and analyzing (*Segmentation, Particle Analysis* and *Calculation*) steps that have been used in this code are all adopted from other computerized image processing projects such as biological visual studies with the same perspective to recognize present regions (e.g., fluid phases) based on visual differences (e.g., colour or shape).

The second part of this paper is dedicated to evaluating the algorithm that is particularly developed in LabVIEW. Performance evaluation has always remained as a major challenge in the design of image processing procedures [85]. This assessment intends to recommend a reliable set of processing steps and adjusted settings for future works that particularly focus on

micromodel image processing/analysis. To achieve this goal, all available methods for segmentation subsequence are implemented in the original algorithm, and then the determined results are compared with the true values that are obtained from the volumetric calculation. Also, the optimized algorithm is utilized both in LabVIEW platform and a popular open-source software, Fiji [59], to process the same images. Consequently, this comparison will highlight the advantages and disadvantages of applying the introduced algorithm in LabVIEW coding rather than a similar commercial platform.

3.3 Material and Methods

3.3.1 Micromodel Structure and Visualization Setup

The visualization setup installed to observe the fluid distributions in micromodel experiments is illustrated in Figure 3-1. In this configuration, a high-resolution camera (Canon 6D) and a 105 mm macro lens are coupled to acquire images during experiments**.** In contrast with visualization systems that use optical microscopes, in this method, the orientation of the camera is more flexible to damp the physical vibration effect and increase the field of view.

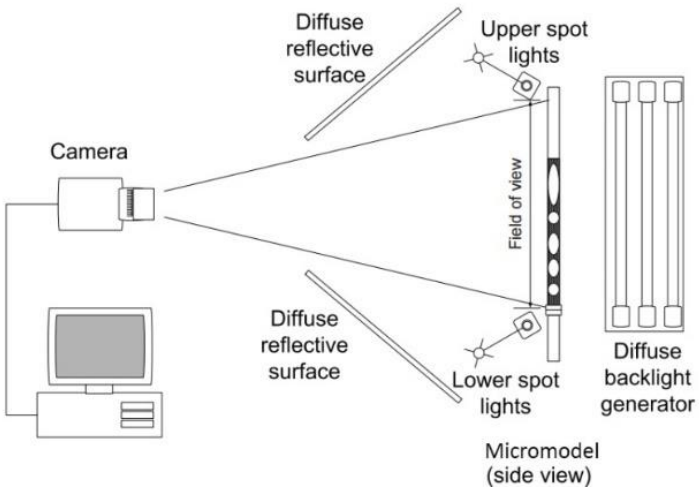

Figure 3-1. Micromodel visualization set-up.

The specifications of the fabricated model used to simulate discussed EOR mechanisms and the injection fluids during the CWI flooding experiment are listed in Table 3-1.

Table 3-1. Micromodels properties and fluid specifications

Micromodel Properties				
Material	**Porosity**	**Pore Size**	**Pore Depth**	**Dimension**
Soda lime glass	0.41	200 - 500 µm	50 µm	200 x 50.7 mm
Injection Fluids				
Carbonated water solution + Methylene blue (1% w/w)		Crude oil		Carbon dioxide*

*The gas phase and no-flow regions (grains) in the micromodel have equal transparency level and are categorized as gas/grain phase.

3.3.2 Programming Algorithm

The custom developed image processing algorithm in this project comprises six essential subsequences (Figure 3-2). They are, in order of execution: *i) Initialization, ii) Monochrome Plane Extraction, iii) Non-Uniform Background Correction, iv) Segmentation, v) Particle Analysis,* and *vi) Calculation*.

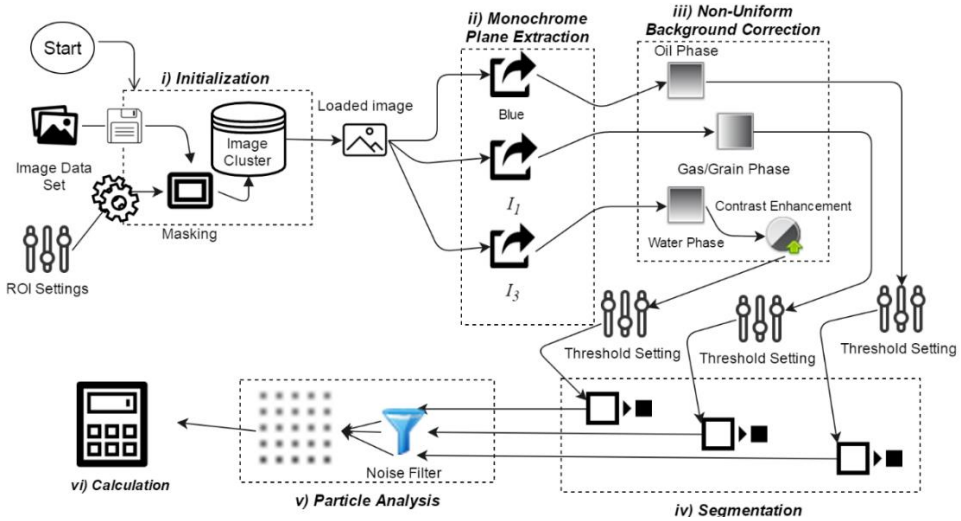

Figure 3-2. Overall programming logical block diagram.

In the initialization step, one or a relevant set of images captured from a particular flooding test is imported to a global cluster. The coherency condition of loaded images must satisfy the following: i) there must be no change in relative position and magnification between the camera and the object (micromodel) and ii) the luminance interruption by external light sources must be minimized.

After loading the images, the region of interest (ROI) for further image analysis is defined for

the first image and formerly applied to the all images in initialized data set. Here, the ROI has a rectangular shape that is manually specified by entering the coordination of four corners. A sample masking procedure's output and the corresponding framework are displayed in Figure 3-3. Furthermore, the LabVIEW block diagram of masking procedure is presented in Figure A-4 (Appendix A).

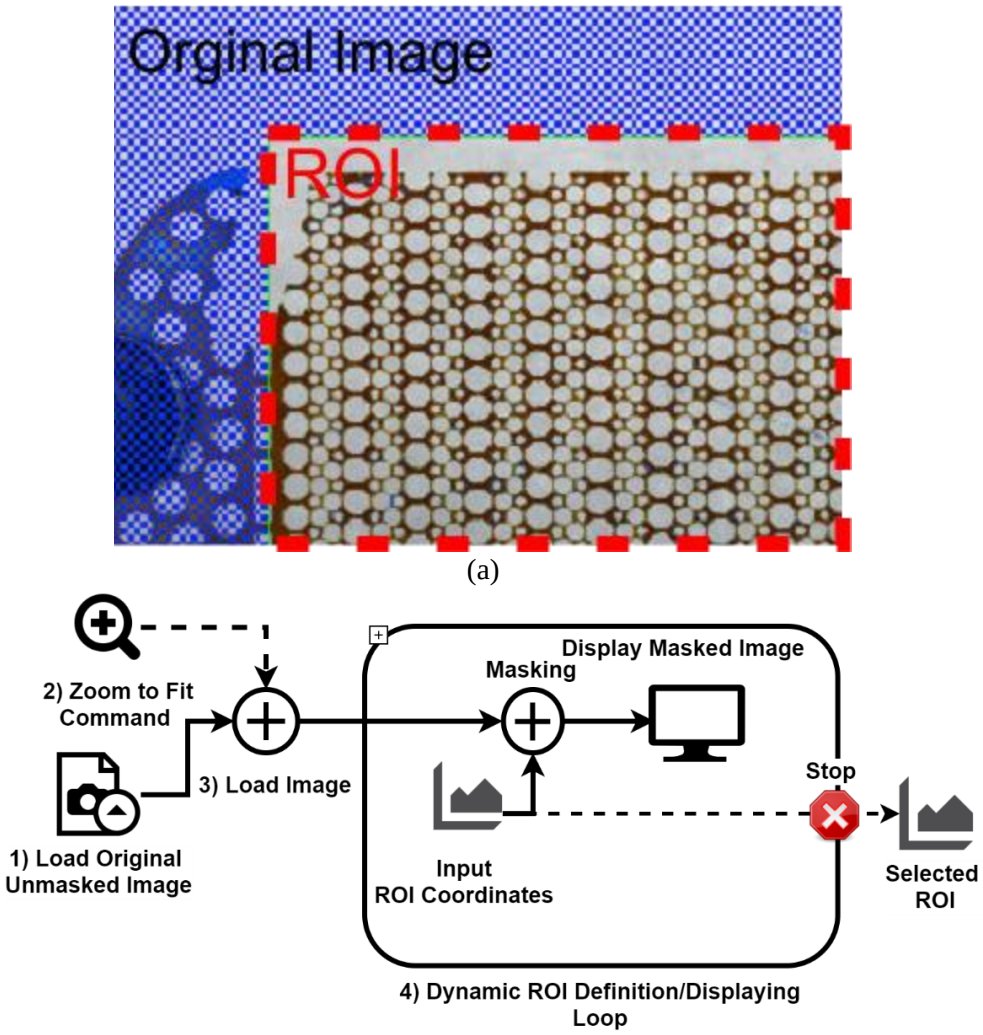

Figure 3-3. Example of ROI definition (a) and developed masking workflow (b).

In the second step (monochrome plane extraction) the initial colour image is transformed into other color spaces and the proper monochrome component for segmentation of each fluid phase is extracted (presented as a gray image). The effect of unbalanced illumination from the backlight in the background is partially corrected in step 3 (non-uniform background

correction). Then segmentation of the corrected gray image is performed in step 4. This step is the main part of the algorithm, which includes a thresholding operation to recognize projected phase regions. Steps 2 to 4 of the algorithm must be repeated for each of the current fluid phases (oil, water, and gas/grain) to adjust the appropriate settings for employed functions with respect to individual chromic characteristics such as intensity range, threshold method and the equivalent gray plane. After configuring the controlling parameters, all the preserved images in the initialized global cluster will be recalled and processed in batch mode to generate binary images for step 5 (particle analysis). This step uses complex image analysis functions to characterize morphological parameters. In the final step (calculation) the mathematical function will perform the post-computation tasks on information measured in particle analysis and quantify fluid flow factors.

3.3.3 Monochrome Plane Extraction

The color image segmentation procedures commonly involve (one or a combination of) monochrome segmentarion approches plus the color space that the understudy image is presented with. Therefore, selecting the best color space to apply the monochrome segmentation on its components is one of the complexities in color image segmentation [86].

The initial image, as shown in Figure 3-4, was acquired from a CWI micromodel injection test and is displayed in RGB colour space. RGB is the most commonly used colour space for pictures acquired by digital cameras modulates the intensity of the three primary components (red, green, and blue) at each pixel [87].

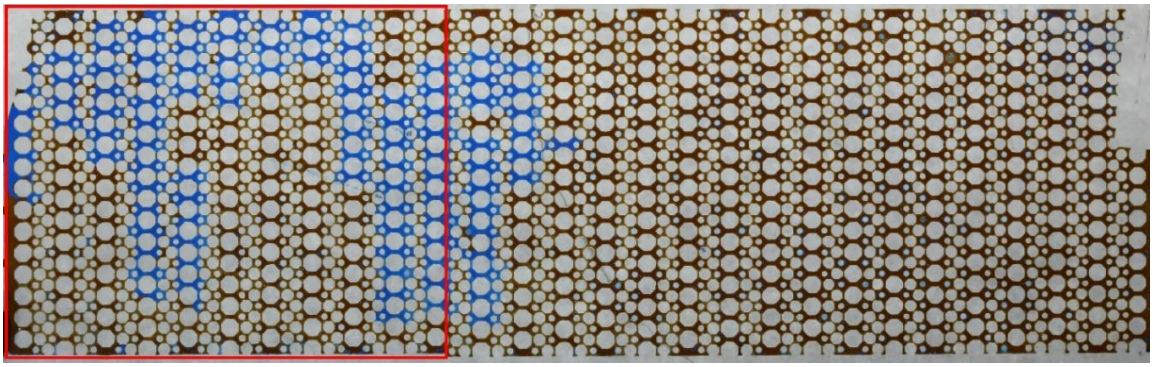

Figure 3-4. An image captured from the CWI test with a sample region of interest (in red rectangle).

The primary R, G, B representative can be transformed to other color spaces with different components (monochrome plane) by utilizing linear or nonlinear transformation techniques. Figure 3-5 illustrates the statistical intensity distribution (histogram) of different color components that are extracted from RGB and HSI-based (HSV and HSL) color spaces. Additionally, matching intensity intervals (also called cluster) with each current fluid phase region (oil phase, water phase and gas/grain phase) during micromodel visualization are highlighted in attributed histograms.

As mentioned above, a successful color image segmentation is the result of choosing the proper monochrome component (from RGB or other transformed color spaces) as well as utilizing the right monochrome segmentation methods. Most of these techniques, for example histogram thresholding (used in this work), perform a better segmentation if the images are composed of discrete clusters (intensity intervals and the corresponding peak values) in the monochrome (gray) histogram while the matching cluster with each object region (fluid phases in this work; oil, water and gas/grain) are perfectly separated by a distinguishable (or deep) valley (high contrast) and have a smooth shape (low noise) [88]. Therefore, based on these conditions, a visual observation on histograms is performed to select the possible representative monochrome plane from the extracted components of pre-defined color systems (RGB and HSI-based systems) and assigned for further segmentation of the flowing phases in micromodel.

These extracted monochrome planes are presented in Figure 3-5. The assessment of the pure components in RGB shows that the Blue plane (Figure 3-5c) represents a well-shaped histogram (note the intense peak for oil phase and the wide smooth valley between this phase and other phases; water and gas/grain) (Figure 3-5k) and has a satisfying agreement with oil phase region in original image. This simple monochrome-equivalent for water and gas/grain phases cannot be adopted directly from pure R, G, or B components. In fact, due to the relative transparency of pixels inside these two-phase regions, there is a high level of correlation among R, G, and B values. This correlation causes all colour components to change similarly for both water and gas/grain phase regions, as a function of illuminated light from the backlight. Hence, this diminishes the overall contrast to a level lower than the required standard level to distinguish proposed phases, as illustrated in Figure 3-5i, 5j and corresponding histograms Figure 3-5a, 5b.

Moreover by observing the HSI-based color systems' components, despite the moderately wide valleys in Hue (H) (Figure 3-5d) and Saturation (S) (Figure 3-5e) planes, the associated histograms indicate a high level of noise that disqualify first two components to be utilized as a base monochrome plane for micromodel images segmentation case (Figure 3-5l and 5m). The third components in the HSI-based color spaces (Value (V), Luminance (L) and Intensity (I)) have a lower level of noise, however, the corresponding peaks to fluid phases in micromodels are not adequately separated for further segmentation (color correlation). This behavior of nonlinear transformed color features (such as HSI-based components) are because of the produced non-removable singularities that means any small perturbation in original RGB image can cause a large jump (noise) in transformed components [89].

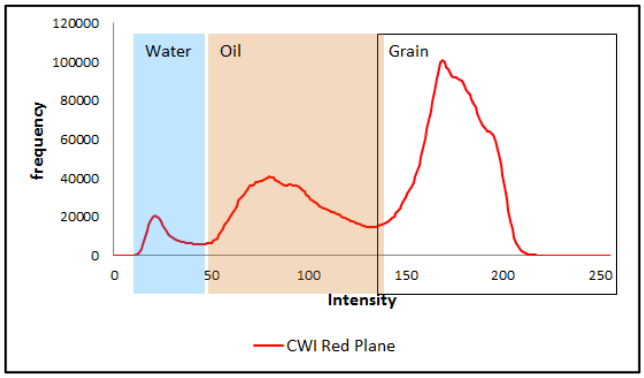

(a) Red histogram

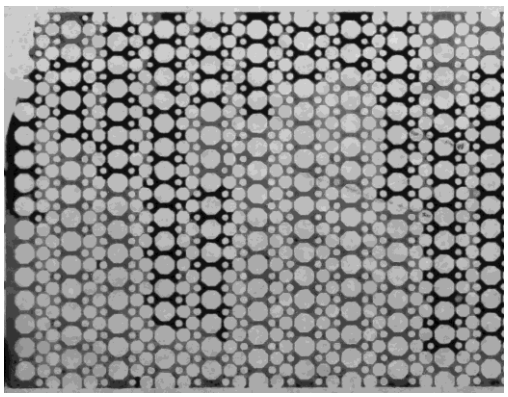

(i) Red plane

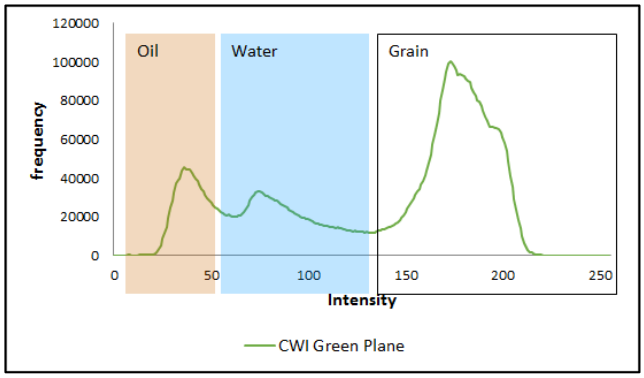

(b) Green histogram

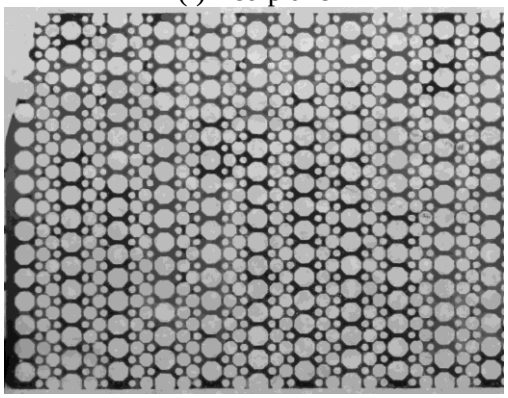

(j) Green plane

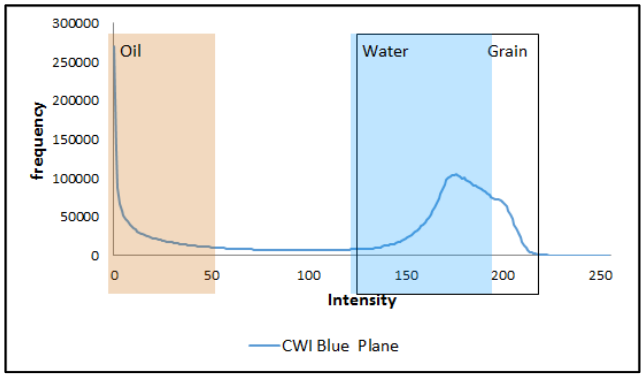

(c) Blue histogram

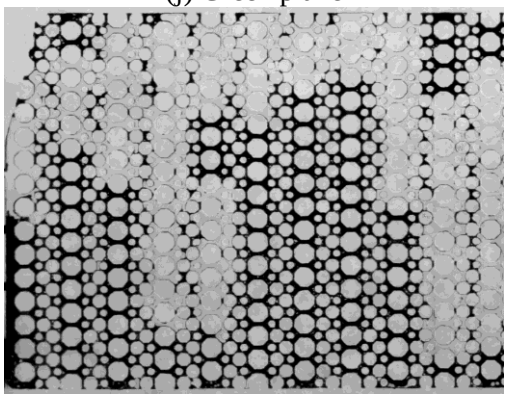

(k) Blue plane

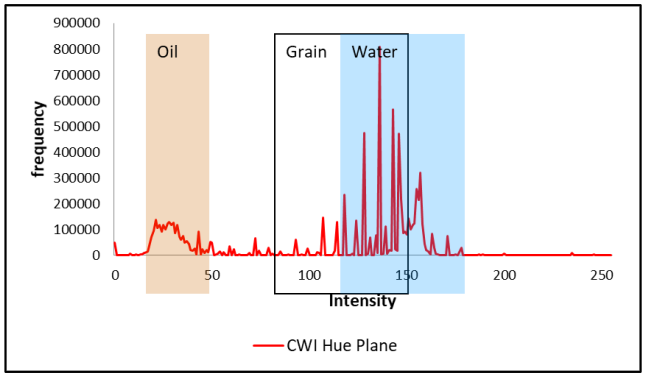

(d) Hue histogram

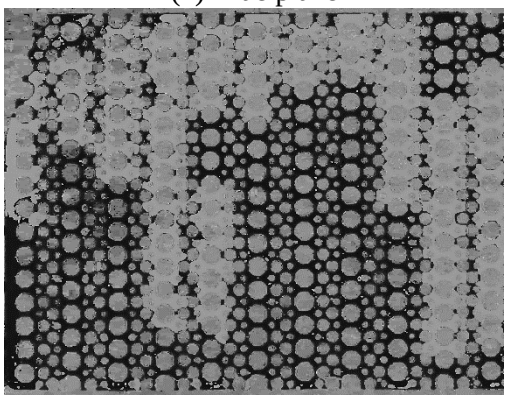

(l) Hue plane

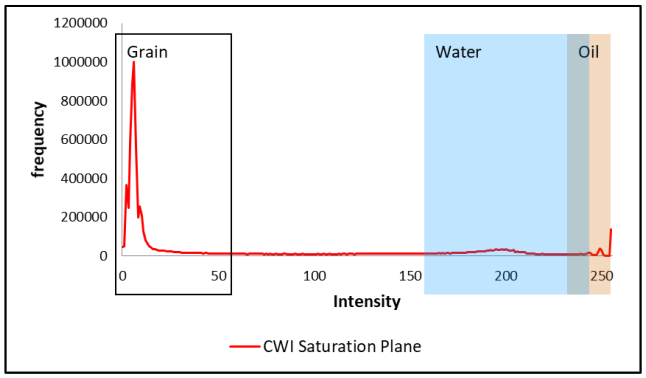

(e) Saturation histogram

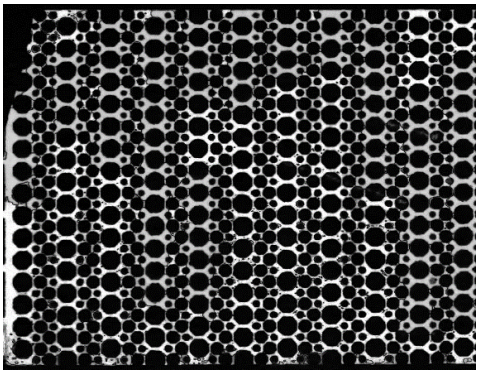

(m) Saturation plane

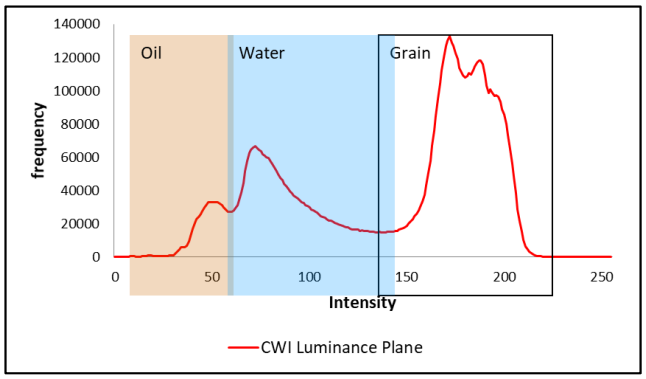

(f) Luminance histogram

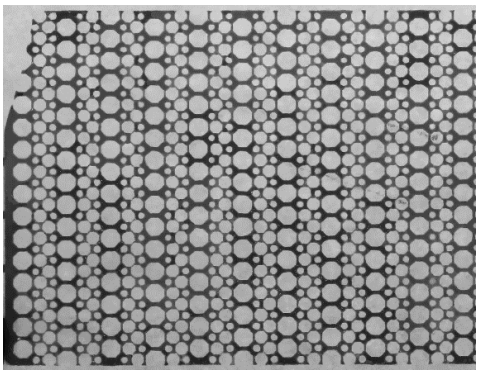

(n) Luminance plane

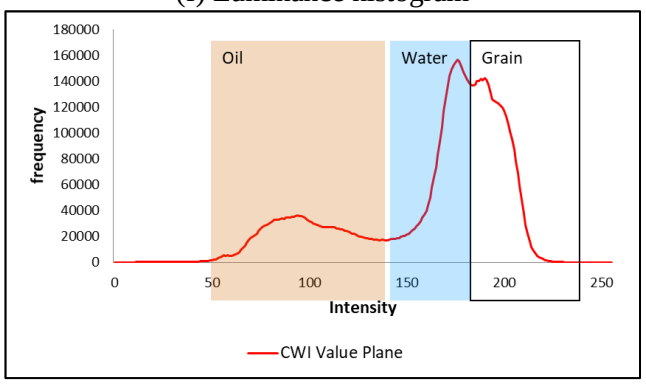

(g) Value histogram

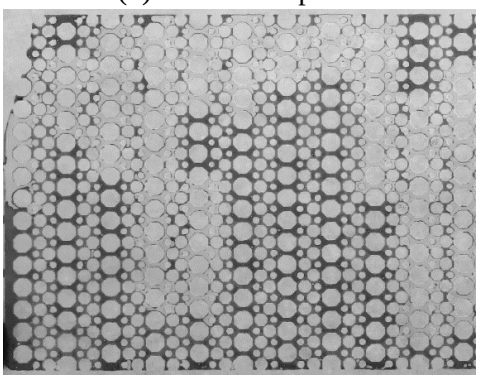

(o) Value plane

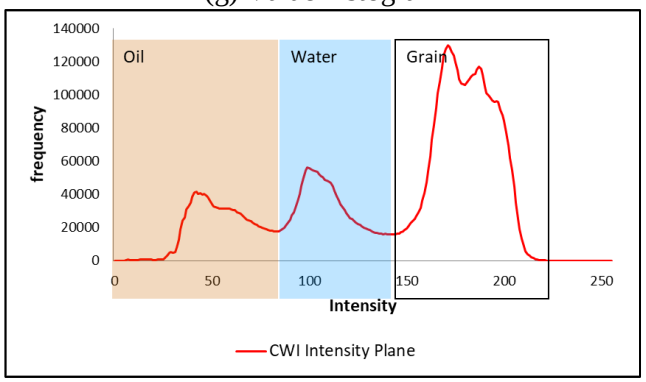

(h) Intensity histogram

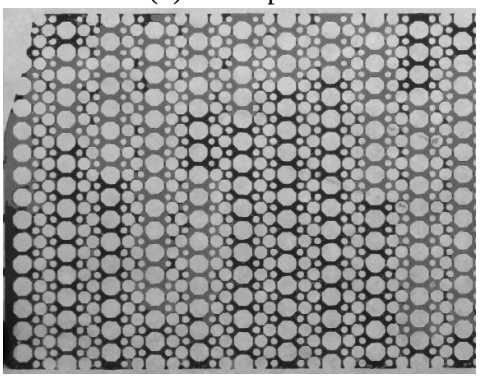

(p) Intenisty Plane

Figure 3-5. Extracted histograms with corresponding colour planes; (a, i) Red, (b, j) Green, (c, k) Blue, (d, l) Hue, (e, m) Saturation, (f, n) Luminance, (g, o) Value and (h, p) Intensity.

To address the issue of spectral correlation between primary colour components or possible

noises after color transformation, many researchers attempted to derive new color features using principal-component analysis (PCA) [90], commonly known as Karhunen-Loeve transformations (K.L) [91, 92] or principal component transformations (PCT). The principal-component technique has been broadly employed in color image applications [93] to segment different regions by deriving a set of new color components which contains most of information from the original RGB components. The first component (PCA_1) is always the most effective component in this transformation. A sample code is developed in this work to perform PCA method over the sample micromodel image and the first two extracted components are presented in Figure 3-6 (MATLAB code is presented in Appendix A).

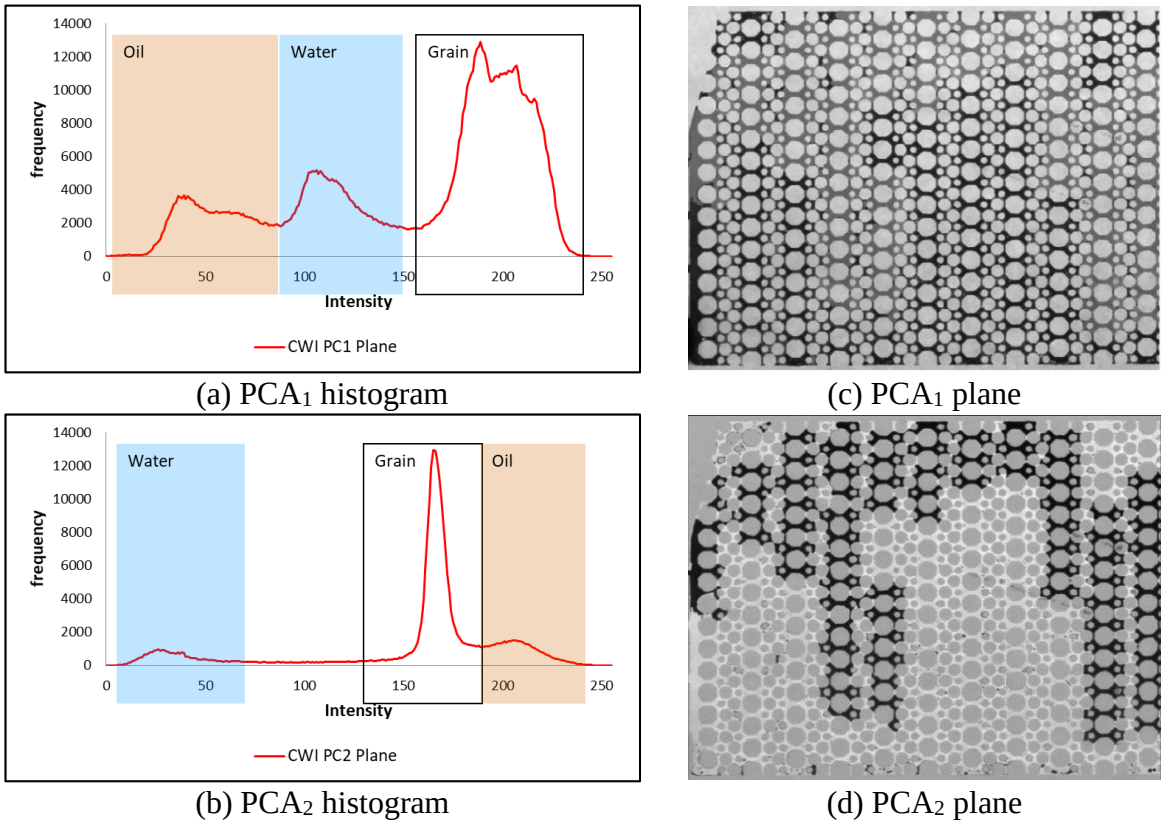

(a) PCA_1 histogram

(c) PCA_1 plane

(b) PCA_2 histogram

(d) PCA_2 plane

Figure 3-6. Extracted histograms with corresponding of PCA colour planes; (a, c) PC_1 and (b, d) PC_2.

Utilizing the PCA method , Ohta (1980), performed a systematic study [94] to extracted 100 different principal components and employed them in a thresholding color image segmentation (similar to our work) and examined the performance of different set of color components. In conclusion the most efficient set of color components for color segmentation purposes is

introduced as follow (only first two components):

$$I_1 = (R + G + B)/3 \quad I_2 = (R - B) \tag{3-1}$$

Looking at the gray images produced using the I_1 and I_2 transformation functions in conjugation with associated histograms (Figure 3-7); the following conclusions are obtained: i) The transformed color components using PCA method have an resembling histogram shape and quality both in this work and in the Ohta (1980) [94] and ii) It can be seen that the I_1 plane (most effective component and approximately similar to the intensity (I) in HSI color transformation) is sufficiently sharp to be segmented equivalently as the Gas/Grain region **(**Figure 3-7a, 7c). Also, the water phase and I_2 plane are almost in agreement; however, because of the low contrast level relevant to the water region **(**Figure 3-7b, 7d), further enhancing corrections have to be applied before thresholding.

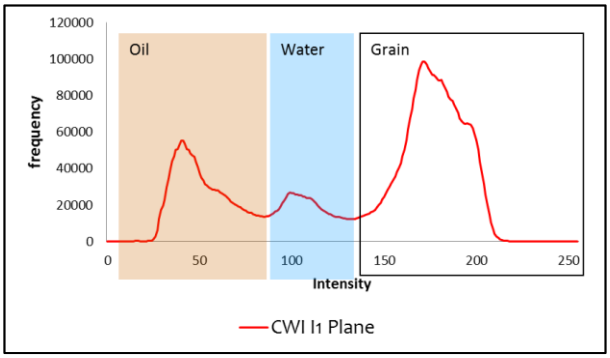

(a) I_1 histogram

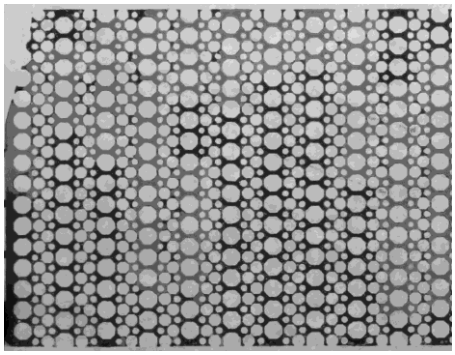

(c) I_1 plane

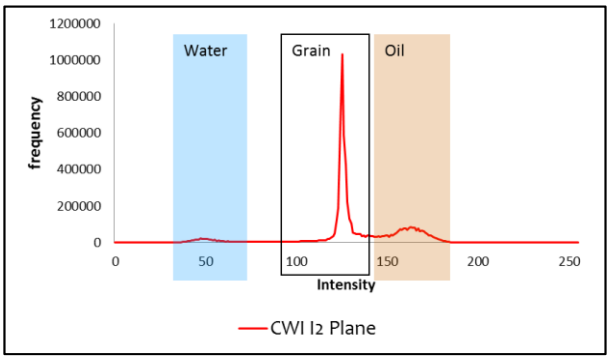

(b) I_1 histogram

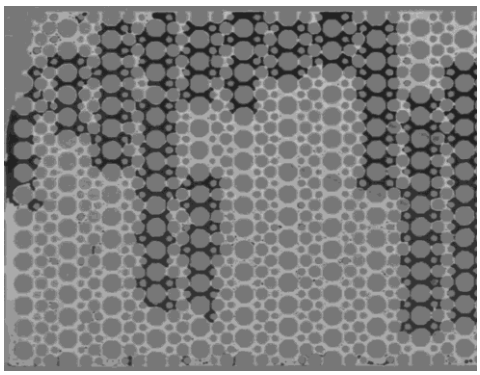

(d) I_2 plane

Figure 3-7. Transformed intensity histograms and corresponding colour planes for (a) I_1 and (b) I_2.

Brightness and contrast are the initial gray image parameters to modify which lead to highlight and/or sharpen fuzzy edges between two neighboring regions before other advanced modifications such as non-uniform background correction.

Figure 3-8 shows the LabVIEW flowchart belonging to the monochrome plane extracting task. For instance, if Plane 1 and 2 are red (R) and reversed blue (-B) respectively, the averaged plane after IMAQ Compare step will provide I_2 plane.

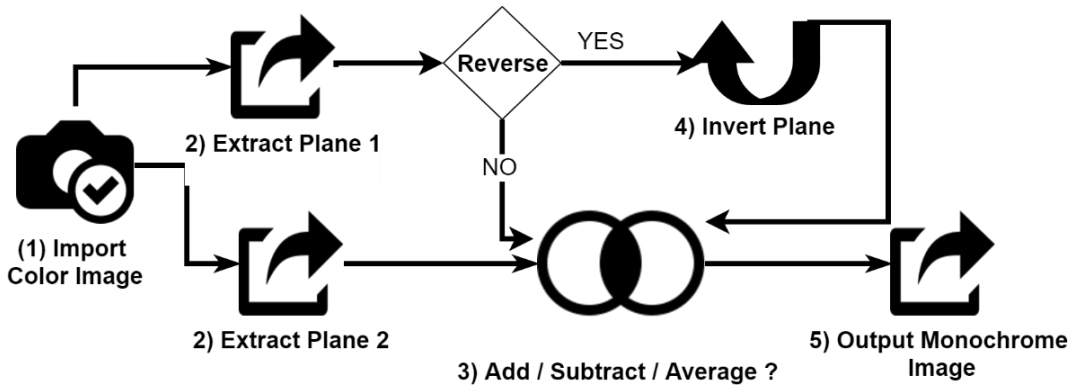

Figure 3-8. Developed flowchart for colour plane extraction.

3.3.4 Histogram Equalization

The contrast of monochrome images can be enhanced using histogram equalization technique to gain an acceptable histogram quality. This step plays an important role in automation of multiple-image analysis by partially adjusting the unbalanced illumination in image background. Histogram equalization technique basically compares every pixel in the input monochrome image with a preset pixel value (an average white intensity in all images) that sets all the pixel values above the set values to be 1 or white in color and others less this value to be 0, or black. Histogram equalization for multiple images processing is an important pre-processing step before thresholding or segmentation and without utilizing histogram Equalization, different threshold values are required for each single image which can delay the automation of the procedure. As an example this technique, a histogram equalization is applied on the extracted Blue planes (Figure 3-9). As it is presented in Figure 3-9, the amplitudes for

various pixels near the center of the image with light backgrounds have been intensified resulting in excessive brightness near the particles that causes the input monochrome become unsuitable for further image analysis steps [95]. Consequently, histogram equalization of monochrome images in this micromodel visualization experiment is only used for I_2 plane that required contrast modification.

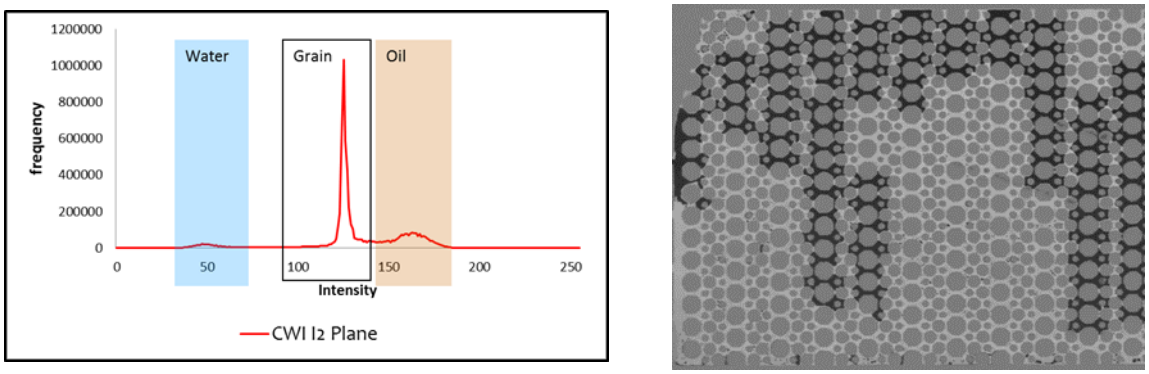

(a) I_2 plane before histogram equalization

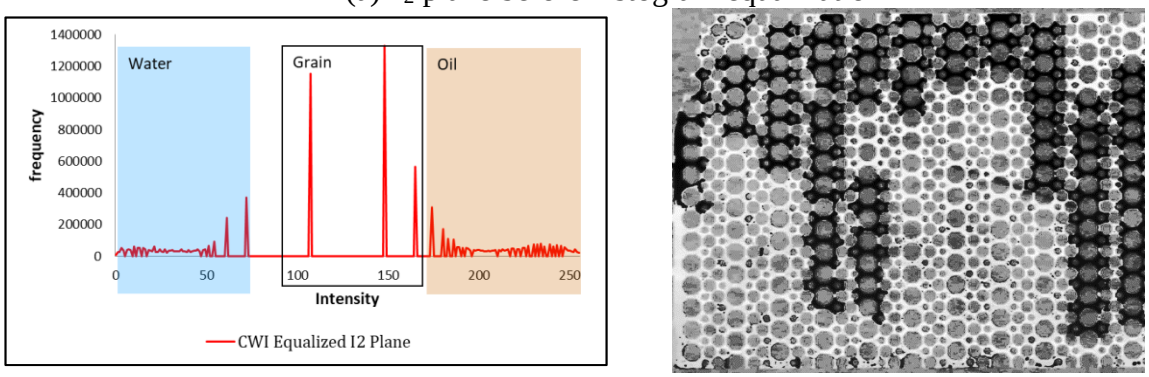

(b) I_2 plane after histogram equalization

Figure 3-9. The histogram and monochrome image of Blue plane; (a) before histogram equalization and (a) after histogram equalization

3.3.5 Non-Uniform Background Correction

A common problem that impedes the technical performance of image-related operations is non-uniform background illumination. In micromodel visualization experiments, this can be due to an unbalanced light metering caused by acquisition apparatuses sensor error, a commercial digital camera, or because of variable light intensity radiated from the backlight**.** This issue can be partially addressed instrumentally by the substitution of fluorescent lamps with LED light sources. Different image processing approaches are proposed in the literature to remove

background heterogeneity to some extent. Singh (2011) introduced a morphological opening resolution; that an approximate non-uniform background is attained and then subtracted from the original image [95]. The influence of this correction for the blue plane is shown as an example in Figure 3-10. In this method, a structure element of similar size and shape to the smallest object in the current image (a geometrically average grain size in the micromodel pattern) is defined, Figure 3-10a. This structural element is then used by two main gray morphological operations, erosion and dilation [96] to construct a non-uniform background, Figure 3-8b. Finally, a new image with the uniform background is generated by subtracting the resulting non-uniform background from the initial image, Figure 3-10c. The graphical comparison between the first and corrected image histograms, as displayed in Figure 3-10d, indicates the effect of morphological non-uniform background removal correction.

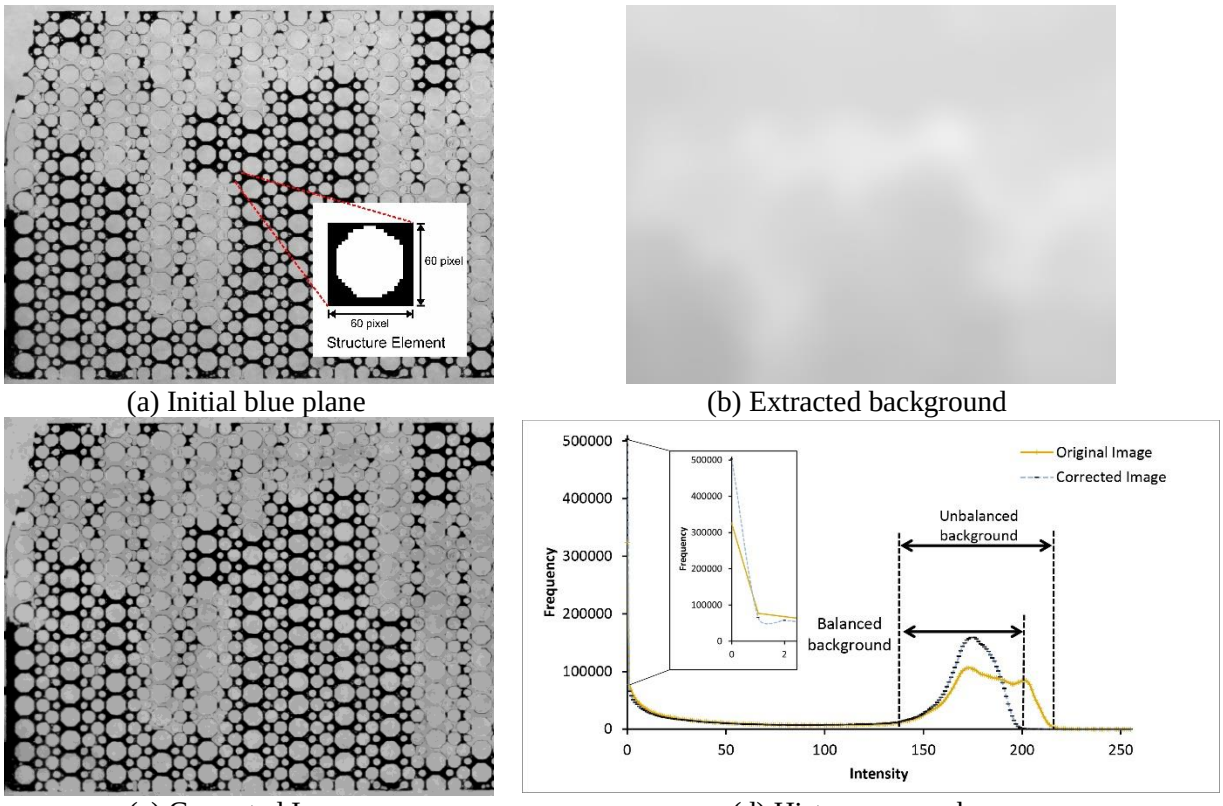

(a) Initial blue plane (b) Extracted background

(c) Corrected Image (d) Histogram graphs

Figure 3-10. Background correction steps; (a) Initial blue plane, (b) extracted background and (c) corrected Image with corresponding (d) histogram graphs.

The developed LabVIEW flowchart to approximate a non-uniform background from the

originally extracted monochrome image is displayed in Figure 3-11. As shown in this framework, the structure element is an input sampling sub-array of [0, 1] integers with a predefined size (60 * 60 pixels here) for both dilation and then erosion steps. After performing these morphological functions, a kernel filter is applied through IMAQ Convolute function to smoothen the sharp intensity transition from dark regions to bright ones, Figure 3-10b. After subtraction of this extracted background from the initial blue plane, the final corrected image is constructed, Figure 3-10c.

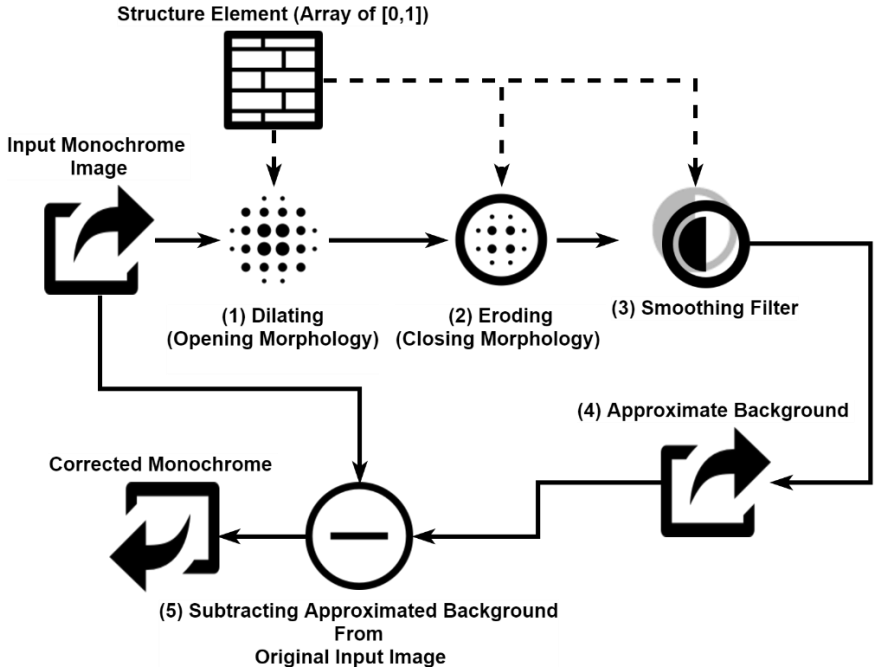

Figure 3-11. Non-uniform background approximation flowchart.

3.3.6 Segmentation

Monochrome segmentation techniques use the homogeneity of existing regions to partition the image. The available methods can be categorized into histogram thresholding, clustering, region growing, and region splitting and merging. Based on its simplicity and an acceptable level of optical contrast between fluids in micromodel, a histogram thresholding approach has mainly been.

The next step in image processing (Figure 3-2) after non-uniform background correction is

image segmentation which can be defined [97]: Dividing the entire image into sub-segments while the segmented regions (S_1, S_2… and Sn) are non-overlapping and the summation of them reconstruct the original image.

There are different forms of image segmentation, for example, thresholding, edge or texture detection methods. As mentioned, the approach to perform image segmentation tasks in this work is thresholding logic which is based on the high contrast observed in images extracted from micromodel flooding tests and the low computational cost of this method.

Thresholding is a simple but practical approach to separate objective pixels (also called foreground), from background pixels, according to the corresponding gray intensity. The output of the thresholding transformation is a binary image $B(x, y)$ as follows:

$$B(x,y) = \begin{cases} 1, & I(x,y) \geq T \\ 0, & I(x,y) < T \end{cases} \quad (3\text{-}3)$$

where T is the thresholding value and $I(x, y)$ is the input image. This value can be adjusted manually, which increases the potential for human error and is a time-consuming task. However, for a large number of images, the threshold value can be automatically computed based on histogram shape. This automatic value can be calculated based on all pixel values, T_{global} or be adapted for each pixel according to neighboring pixels, $T_{local}(x, y)$ [98].

The literature contains a great number of comparing surveys which introduce and revise the available thresholding methods with different applications. Sezgin (2004) provided an overview of the optimization function and error score of thresholding algorithms offered by the IMAQ toolbox [99] and shown in Table 3-2.

Table 3-2. Quantitative evaluation of available thresholding methods in LabVIEW IMAQ toolbox.

Method Name	**Optimization Function**	**Average Error Score** $(S_{\bar{E}})$*
Cluster_Otsu [100]	Global minimizing of the total within-region variances for background and foreground.	0.318
Entropy_Li [101]	Maximizing the total entropies in foreground and background regions.	0.346
Niblack [102]	Adopting local threshold value based on standard deviation $\sigma(x,y)$ and mean $m(x,y)$ values of surrounding pixels with a size of $b\times b$. $T(x,y)=m_{b\times b}(x,y)+k.\sigma(x,y)$, where k is the sensitivity factor.	0.638
Background Correction (Local_White) [102]	Comparing intensity $I(x,y)$ with local mean value over a window size of $b\times b$ pixels. $T(x,y)=\begin{cases}1 & if\ I(x,y)\geq k.m_{b\times b}(x,y)\\ 0 & if\ I(x,y)<k.m_{b\times b}(x,y)\end{cases}$	0.665
Moment_Tsai [103]	Preserving the total moments of regions in binary image equal to the total value in the original image.	0.484
Metric	Approximating the threshold value based on histogram shape and searching for distanced peak values belonging to foreground and background.	NA

* The quantitative average error score $(S_{\bar{E}})$ given in this table is calculated by arithmetic averaging of the performance of each technique over 40 different image samples and a higher value (maximum =1) represents more error in thresholding.

3.3.7 Particle Analysis and Calculation

The next step of the image processing procedure (Figure 3-2) is designed to analyze morphological features belonging to segmented particles, in a binary image generated from thresholding [104]. Figure 3-12 illustrates the steps required to perform particle analysis. First, possible noise created through previous conversions is reduced using morphological filtering operations. In morphological filtering, the particle area criteria defining noise is set value defined by user. Therefore, any particle with an area size less than this criterion value (0.0001% of total image size in this work [105]) is removed from the binary image. After noise filtration step, the geometrical properties of the remaining identified particles are measured individually.

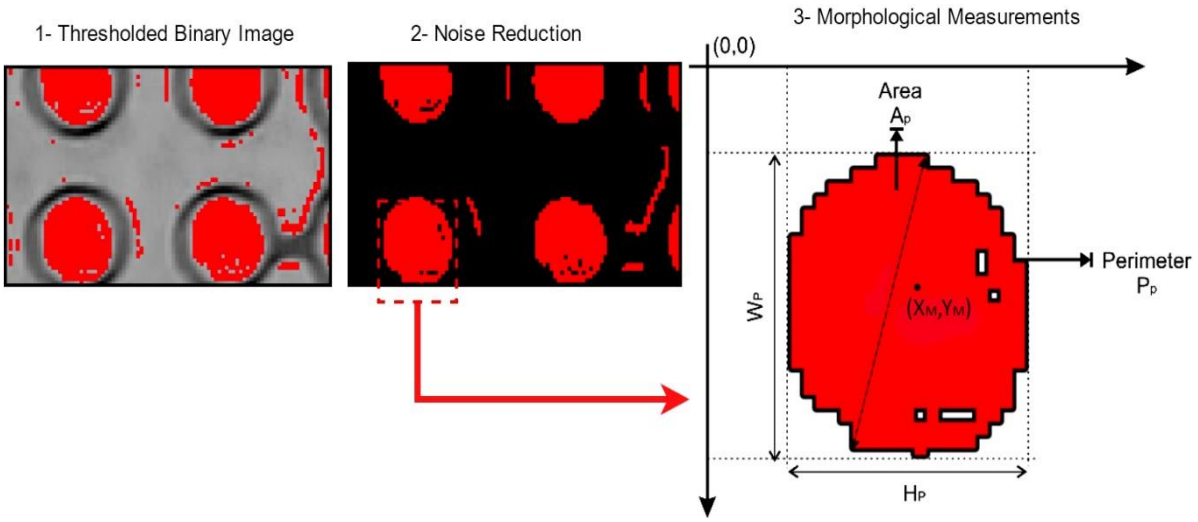

Figure 3-12. Schematic steps of particle analysis.

The major morphological particle measurements, established by IMAQ Particle Analysis function, are the area A_P, perimeter P_P, dimension $[W_P, H_P]$ and center of mass coordination $(X_M, Y_M)_P$ of each isolated particle. Practically, the properties measured by this function are the input information needed for calculations step. The mathematical functions that quantify the variables such as phase saturation, size distribution and image analysis error are implied in calculation step.

3.4 Results and Discussion

3.4.1 Thresholding Performance

In addition to the assessment of thresholding performance presented in Table 3-2, the segmentation ability of the methods employed specifically to interpret the case study micromodel images was examined via misclassification error (*ME*) [67].

Misclassification error of a segmented image is defined as:

$$ME = 1 - \frac{|B_O \cap B_T| + |F_O \cap F_T|}{|B_O| + |F_O|} \qquad (3\text{-}4)$$

where F_O and B_O represent the foreground and background regions in a human-segmented

image while F_T and B_T denote foreground and background regions extracted by the thresholding algorithm. More specifically by this measure, the thresholded image is compared with a ground-truth image as a certain reference (usually generated by Adobe Photoshop under human supervision [67]), and then the percentage of pixels incorrectly assigned to background or foreground is calculated.

To compare the efficiency of all available thresholding methods, the *ME* associated with segmentation of images collected during primary water flooding in CWI experiments was computed separately for available three colour phases and is shown in Table 3-3.

Table 3-3. The average misclassified error of thresholding methods over CWI experiment

Phases	**Background**	**Local Thresholding**		**Global Thresholding**			
		Background Correction	Niblak	Cluster_ Otsu	Entropy_Li	Metric	Moment
Gas/Grain	corrected	0.096	0.041	**0.007**	0.051	0.025	0.516
	not corrected	0.096	0.041	0.018	0.072	0.035	0.639
Water	corrected	0.093	0.077	0.044	0.131	**0.001**	0.564
	not corrected	0.096	0.335	0.046	0.146	0.004	0.572
Oil	corrected	0.042	0.106	0.035	0.204	**0.010**	0.272
	not corrected	0.048	0.113	0.041	0.206	0.026	0.290

Comparing the *ME* values in Table 3-3, it can be observed that the optimized method with the lowest *ME* value (denoted by bold numbers in Table 3-3) for oil and water phases is metric and clustering is the optimal method for gas/grain.

The *ME* term evaluates the thresholding result for an individual phase in the image. Therefore, to estimate the overall segmentation performance which is directly proportional to the summation of individual thresholding errors of all three phases, a custom scale is defined as follows to address the total uncertainty of threshold (*UT*) pixels that are placed at the

intersection of two or more different phases (a) plus the non-detected pixels (b) :

$$UT = \underbrace{\left(\frac{|S_w \cap S_o| + |S_G \cap S_o| + |S_w \cap S_G|}{I}\right)}_{a} + \overbrace{\left(\frac{I - |S_w \cup S_o \cup S_G|}{I}\right)}^{b} \tag{3-5}$$

where S_w, S_G and S_o are the water, gas and oil phase segmented regions in a typical micromodel image with a size of I. The greater value of UT denotes a higher number of pixels that are attributed to more than one phase or do not belong to any phase, Figure 3-13.

The optimized thresholding methods with minimum ME values were applied to segment three phases in a set of water flooding images. As shown in Figure 3-14, the resulting total uncertainty values are distributed around an average value (approximately 0.01) without any systematic trend.

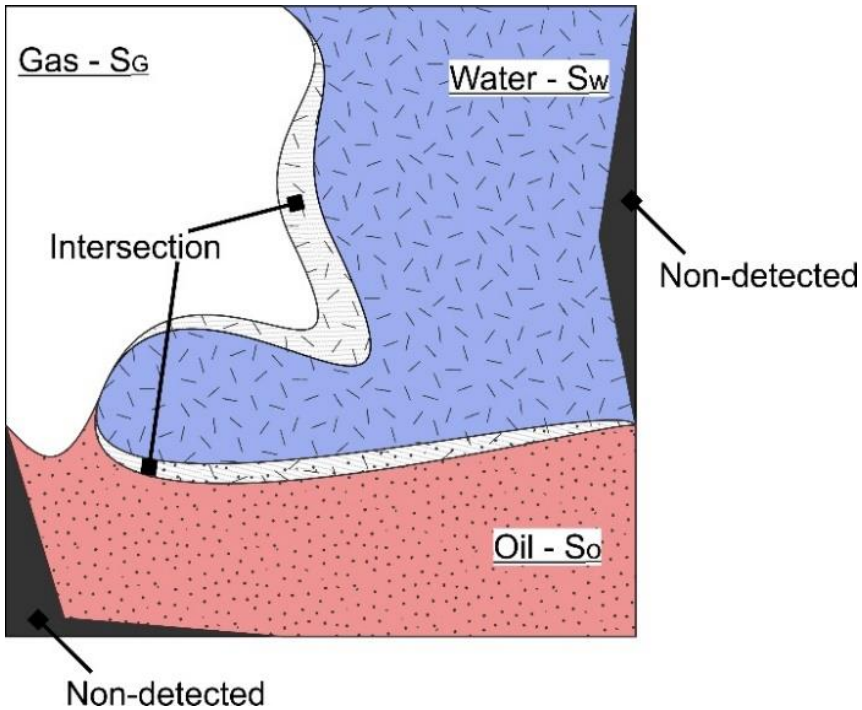

Figure 3-13. The schematic definition of the uncertainty of thresholding.

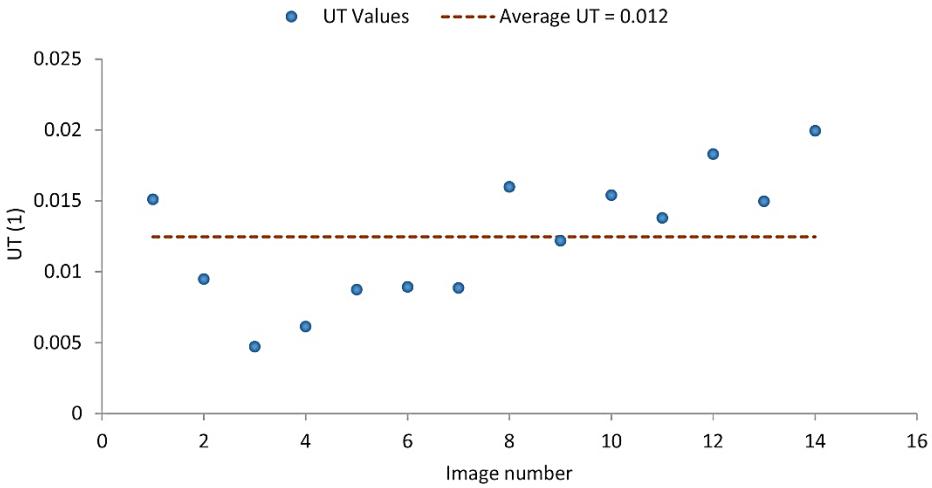

Figure 3-14. The UT values of a sample water flooding test.

To verify the performance of the optimized image segmentation algorithm, the volumetric saturations of oil and water, calculated by the material balance in a micromodel through subtraction of the dead volume and produced oil from total injected volume of water, are compared with measured optimized image-based saturations, Figure 3-15.

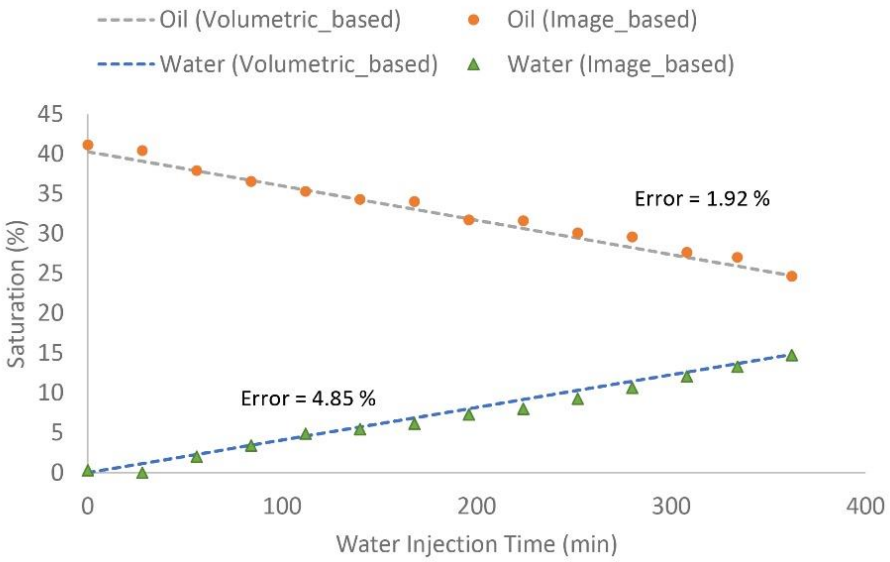

Figure 3-15. Volumetric and image-based measured saturation

3.4.2 Overall application evaluation

As mentioned in the introduction, the capability of LabVIEW to run the optimized algorithm is compared with the Fiji software to analysis a sample micromodel image data set (10 images).

Fiji, a popular platform originally focused on biological-image studies, has the required functions to complete the similar tasks associated with the discussed image processing framework (Figure 3-2) which aim to segment a multi-region image. The evaluation results after running the same algorithm on the same input image data set (10 images) corresponding to the LabVIEW and Fiji software are listed in Table 3-4. These terms are general criteria to assess the level of accessibility, being user-friendly and applicability in petroleum visualization filed that the developed program can offer in comparison with Fiji for similar purposes.

Table 3-4. Methodology Evaluation

Feature	LabVIEW	Fiji
Running Time	+ < 1 min (in parallel mode) per image	- 10 min per image
Processing Mode	+ Parallel/Series image processing	- Only series image processing
Available Thresholding Methods	+ local, automatic and manual categories	- local thresholding option is available
License	- Required	+ Free
Post-processing of Raw Data	+ Internal mathematical module is included for image-data analysis	- External calculator (EXCEL) is needed
Principal Components Analysis	- In-house programming is needed for PCA analysis	+ Online Plugin for PCA analysis is available
Connectivity to Camera	+ Directly connected to camera for dynamic analysis	- Only static image analysis

The possibility of parallel image processing in LabVIEW reduces the running time to less than a minute and also provides the opportunity to detect multi-phases at the same time. This feature can be a great advantage in a micromodel experiment which produces a large number of images in a short period. Additionally, the dedicated thresholding options in Fiji do not include local thresholding methods such as Niblack which might be useful for discrete fluid-phase detection purposes (gas bubbles).

The free licensing alongside with available open-source libraries are the key advantages of Fiji which can be used for simple visual data analysis.

3.5 Conclusions

Most studies that focus on screening the proposed enhanced oil recovery mechanisms in micromodels have employed qualitative methodologies to compare and observe existing interaction between contributing factors. However, as presented in this research, the new improvements in available visualization equipment and computational techniques can provide an opportunity to obtain quantitative data from these experiments. Following this perspective, a major part of this paper was dedicated to validating the extensive capability of LabVIEW to process and analyze image data extracted from a visual investigation of fluid-fluid displacement phenomena in micromodels.

In the first stage, the required techniques to proceed the designed algorithm's steps (masking, background balancing, contrast/brightness/gama values correction and thresholding) were adopted from relevant image processing technical resources. Next, the controlling parameters of first three steps were adjusted to the nature of captured images during micromodel multi-phase displacement experiments. Following this primary adjustment, two proper mathematical measures, misclassification error (ME) and uncertain thresholding (UT), were used to quantify the performance of alternative thresholding methods and then optimize the parameters of an algorithm based on feedback. The misclassified error results calculated in this paper show that each of the flowing fluids has a unique segmentation scenario based on its optical properties. The coloured water and oil phases with relative lower light transparency have shown the minimum error (< 1.0 %) within Metric while the gas/grain phase has a higher accuracy with Cluster_Otsu technique. It is also shown that the non-uniform background correction reduces the misclassified error, which leads to improving the accuracy of segmentation. The robustness of the overall adjusted algorithm was confirmed by low average percentage (1.2 %) of uncertainty.

As the second stage, a ground truth evaluation through a sample water-oil displacement test was performed by comparing the saturations of fluids that are obtained from both volumetric balance and image processing method. The acceptable level of agreement between volumetric and image-based extracted saturation from micromodel images supports the reliability of discussed image processing/analyzing approach in microfluidic flow studies. Finally, the efficiency of NI platform to implement current, or possibly future, image processing code was indicated by a comparative examination with similar commercial software called Fiji. The overall result of this comparison highlighted the unique capability of LabVIEW to execute the in-house developed image processing applications that explicitly can meet the requirements of EOR visualization tests in micromodels.

CHAPTER 4
CONCLUSIONS SUMMERY AND FUTURE WORK

Through this thesis, two frameworks are recommended that aim to promote the quality of micromodel visualization experiments with respect to the requirements of Enhanced Oil Recovery (EOR) screening projects.

Firstly, a technical modification to improve the feasibility of the wet etching micromodel fabrication process is suggested to reduce total time and operational costs and enable this method to manufacture larger models with a flexible network pattern. The capabilities of the final constructed model are evaluated under mid-pressure EOR displacement tests.

Secondly, an advanced visual interpretation algorithm is adopted from image processing literature and written through a graphical-based platform offered by National Instrument (NI). The controlling parameters in this algorithm are optimized based on the visual features and fluid configuration of present phases, such as oil and colored water. This optimization was obtained by minimizing the deviation of image analysis-based calculated values from true values that are obtained from volumetric material balance.

4.1 Conclusions

- The new laser-engraving procedure in wet etching method offers more flexibility in the design of complex network patterns, while the fabrication time is decreased. The direct conversion of rock's pore images to the importable laser files allows fabricating a wide range of patterns while the masking time by laser machine (less than one hour) is significantly less than masking by photoresist/UV lithography (approximately 1 day).

The related costs to photoresist/UV lithography masking, such as coating material, clean-room preparation, UV light safe area and spinning coater are waived.

- The resulting mirror (glass) plate after the laser masking step shows an adequate stability in etching buffer. The adjustable power and speed of the CO_2 laser machine allow this approach to mask a broad range of mirror products with variable thickness and coating material.
- The chemical and physical strength of the fabricated micromodel is validated and confirmed to be applicable in EOR displacement tests under moderate pressure range ($\leq$ 500 psi).
- The image processing techniques utilized to develop the algorithm for micromodel visual data interpretation are adopted from similar image-based quantification studies. However, the order and governing factor of implemented sequences are adjusted based on the fluid phases' visual features.
- The viability of LabVIEW as an advanced programming platform, to run the proposed image processing algorithm is validated in this research. There are other available software, commercial and programming-based, that provide a vision library which offers a set of widely-used functions to transform, modify and quantify the images. However, the performed comparison of LabVIEW and Fiji (a comparable commercial image processor), illustrated that LabVIEW has more capability to analyze the obtained visual information from micromodels.
- The related error to image processing techniques can be determined by different available mathematic and experimental approaches. Here, the misclassification error (ME) and threshold uncertainty (UT) are error measurements applied to evaluate the performance of the different configurations for the original algorithm and to optimize the controlling parameters. The image processing results are compared with the

estimated values from experimental methods. The low deviation between these two datasets confirms the capability of proposed algorithm along with the ability of LabVIEW to perform large visual computation tasks.

4.2 Suggestions for future work

- The operating pressure of displacement tests is restricted by the physical strength of the used mirror (glass) in model fabrication. Therefore a stronger glass material, such as sapphire or quartz can be replaced with regular soda lime. However, the mirrors with stronger glass material are significantly more expensive and require higher bonding temperature.
- The introduced algorithm in this research is designed to import a large image dataset in static mode. The next version of this code can be improved to operate in a dynamic mode, which means to capture/process the continuous visual data. Dynamic data computation provide the opportunity to investigate the mechanisms with a higher conversion rate. The virtual converter functions, offered by LabVIEW, can extract individual frames (images) from the recorded (or live) video and feed them to the developed static. The major challenge in this modification is that the resolution (quality) of sequenced images is lower than separately captured images. This issue requires the advanced cameras with faster frame per second and a powerful CPU to run the parallel sequencing and image interpretation tasks.

APPENDIX A
IMAGE PROCESSING LABVIEW CODE

A.1 Algorithm structure

This Appendix represents the in-house image processing code (VI) in LabVIEW 2016 workspace, which aims to import, process and quantify micromodel images. The logical structure of this VI is explained, and the related algorithm is discussed step by step including the corresponding graphical illustration.

The overall workflow in this algorithm comprises four main steps: (in order of execution) *i) Initialization, ii) Phase Definition, iii) Batch Calculation and Data Export* (Figure A-1).

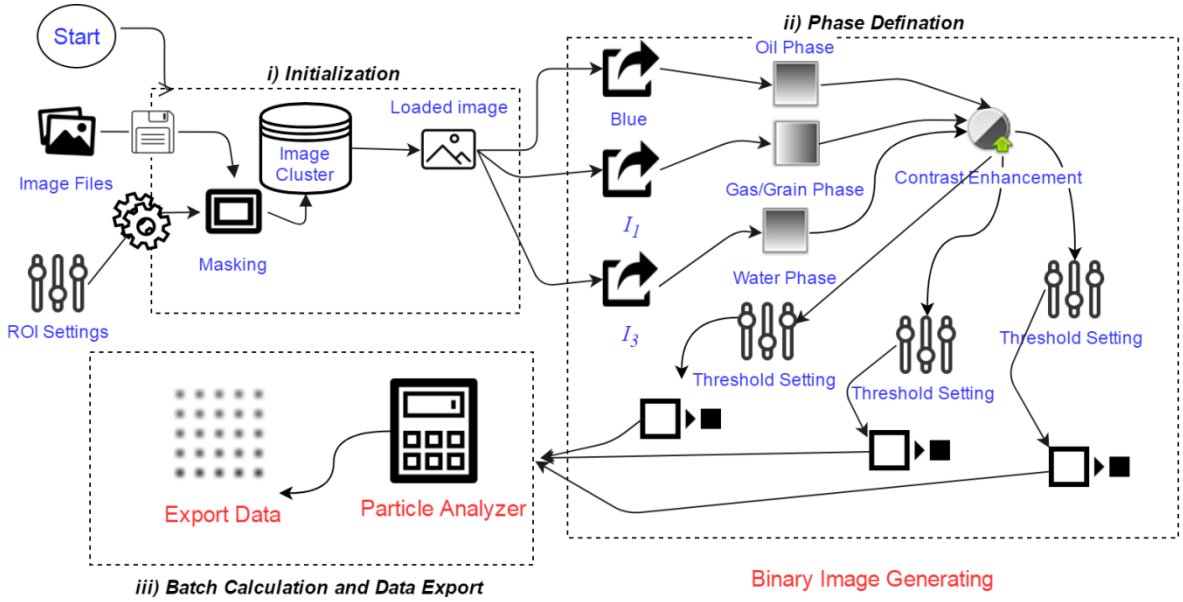

Figure A-1. The logical diagram of the HiberniaImgPro algorithm.

A.2 VI Documentation

The LabVIEW project file manager that shows all contributing subVIs and global variables in the main VI is displayed in Figure A-2.

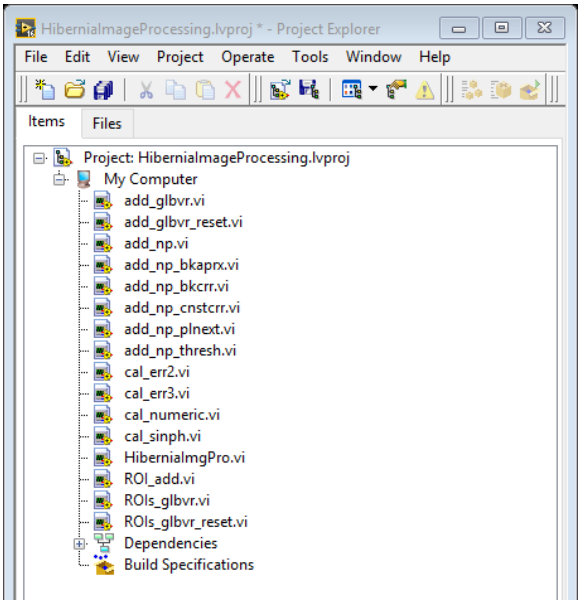

Figure A-2. The file explorer of Hibernia Image Processing project.

The presented objects in the HiberniaImageProcessing.lvproj's file explorer window are briefly discussed in Table A-1.

Table 4-1. The description of global values and subVIs in the HiberniaImgPro project.

Name	Algorithm Step	VI Function
ROI_add.vi	Initialization	Define a region of interest.
ROI_glbvr.vi	Initialization	Save the defined ROIs.
add_np.vi	Phase Definition	Define a new phase.
add_np_plnext.vi	Phase Definition	Extract a monochrome plane.
add_np_bkaprx.vi	Phase Definition	Approximat the original background.
add_np_bkcrr.vi	Phase Definition	Correct the new background.
add_np_cnstcrr.vi	Phase Definition	Modify the image contrast.
add_np_thresh.vi	Phase Definition	Threshold the processed image.
cal_numeric.vi	Calculation & Data Export	Calculate the sample image parameters.
cal_err3.vi	Calculation & Data Export	Calculate the misclassification error.

A.2.1 Initialization

i. Import image files:
(HiberniaImgPro.vi/event structure <Import Image frame>)

This event structure's frame imports images and saves their addresses in a local value (Image Paths) is presented in Figure A-3.

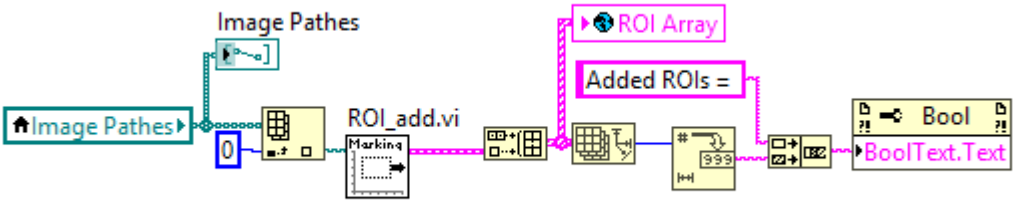

Figure A-3. The <Add Image> frame of event structure.

ii. Define Region of Interest (ROI):

(HiberniaImgPro.vi/event structure <Import Image frame> /ROI_add.vi)

The front panel and the block diagram related to ROI_add.vi is displayed in Figure A-4. This subVI's objective is to extract a rectangular region of interest from the original image. Next, the coordination and angel of the defined ROI are saved in a global variable (ROI_glbvr.vi) (Figure A-3). The introducing a new ROI can be repeated 'n' times which will lead to initiate 'n' parallel computation processes.

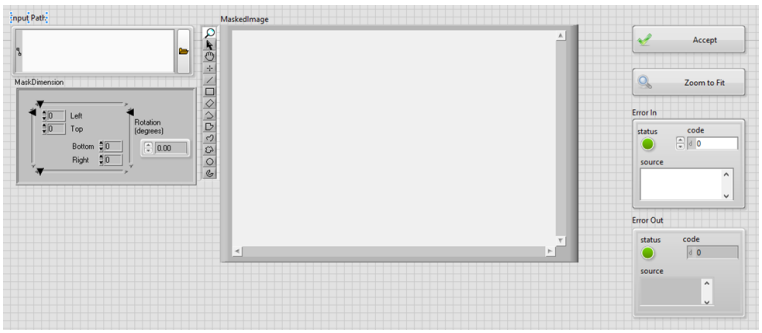

(a) Front panel of ROI.add.vi

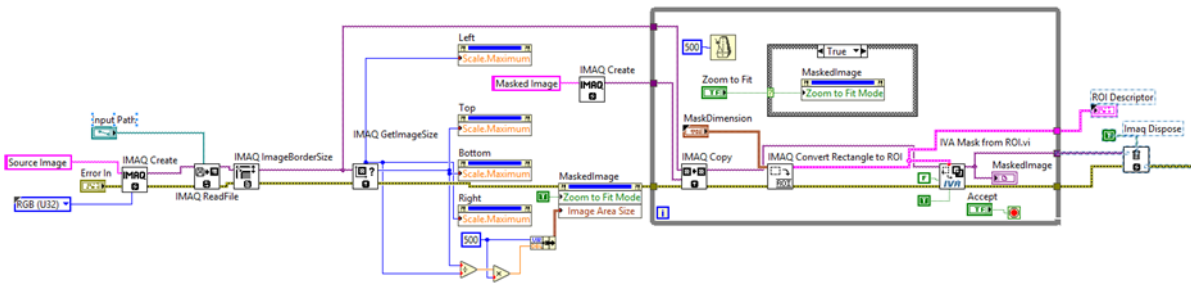

(b) Block diagram of ROI.add.vi

Figure A-4. The LabVIEW VI for the definition of ROI (ROI_add.vi).

A.2.2 Phase Definition

i. Add a new phase:
(HiberniaImgPro.vi/event structure <Add New Phase >/add_np.vi)

This event structure's frame is dedicated to execute the phase definition subVI (add_np.vi), is showed in Figure A-5.

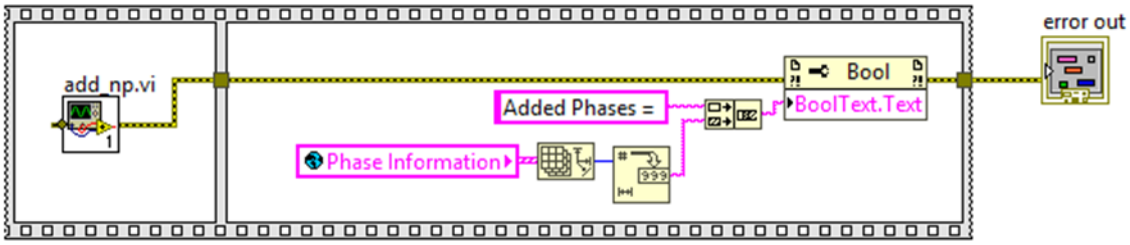

Figure A-5. The <Add New Phase> frame of event structure.

This subVI aims to set controlling factors of four main sequences of image processing algorithm (refer to Section 3.3.2 Programming Algorithm, Figure 3-2). As illustrated in Figure A-6, these sequences (1-Monochrome Plane Extraction, 2) Non-Uniform Background Correction, 3) Brightness/Contrast/Gama Correction and 4) Segmentation) are implemented in a four-frame flat sequence structure.

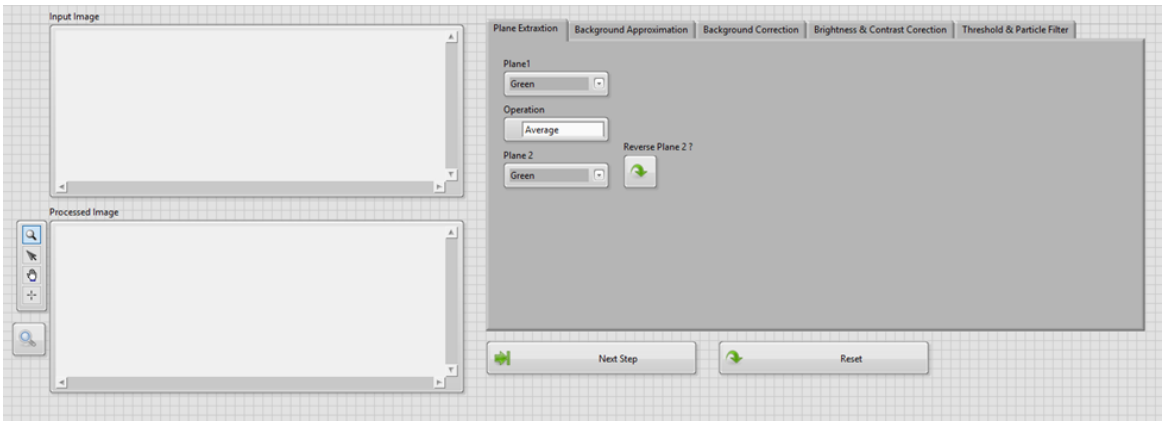

(a) Front panel of add_np.vi

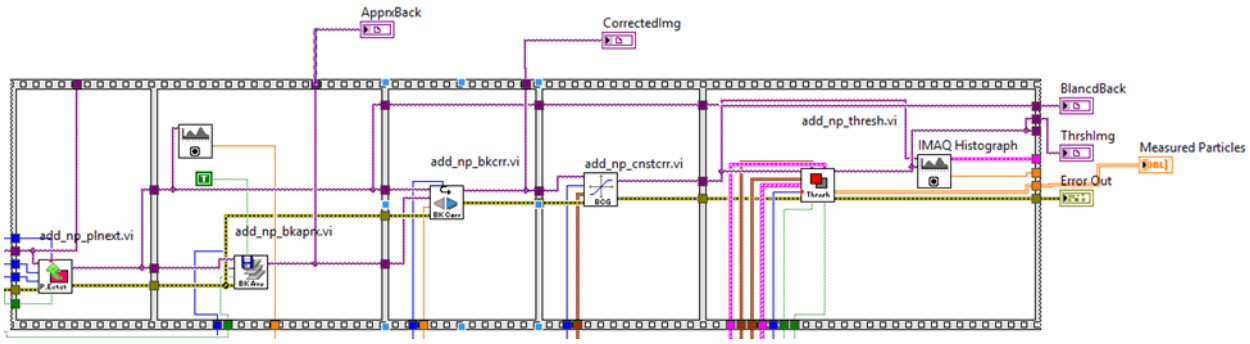

(b) Block diagram of add_np.vi

Figure A-6. The LabVIEW VI for the definition of a new phase (add_np.vi).

a. Plane Extraction:
(HiberniaImgPro.vi/event structure <Add New Phase >/add_np.vi /add_np_plnext.vi)

This subVI extract an equivalent gray plane form original full color image. The front panel and block diagram of this task is demonstrated in Figure A-7.

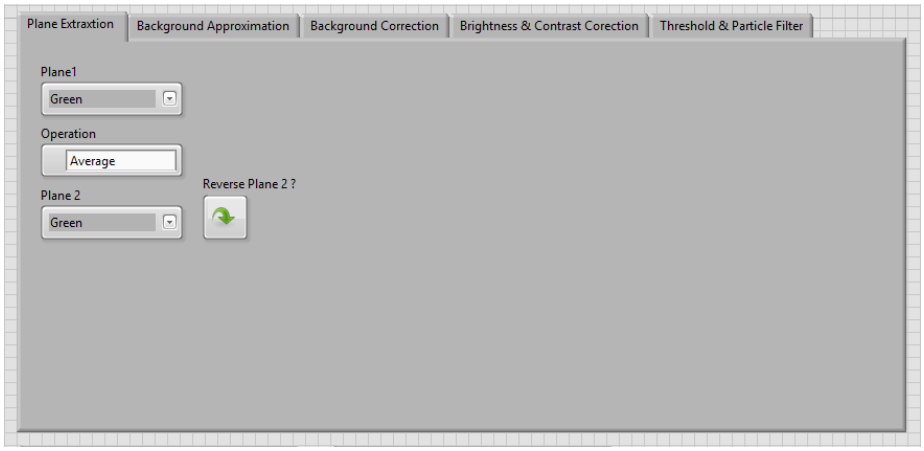

(a) Front panel of add_np_plnext.vi

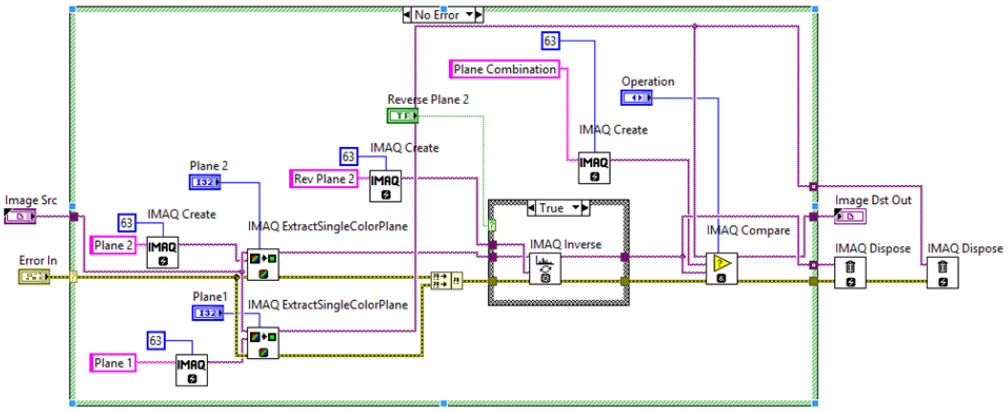

(b) Block diagram of add_np_plnext.vi

Figure A-7. The LabVIEW VI for monochorome plane extraction (add_np_plnext.vi).

b. Non-Uniform Background Correction:
(HiberniaImgPro.vi/ event structure <Add New Phase >/add_np.vi/add_np_bkaprx.vi & add_np_bkcrr.vi)

This step includes two subVIs which aim to approximate an average background and then correct the non-uniform background with this approximation. The corresponding front panels and block diagrams are displayed in Figure A-8.

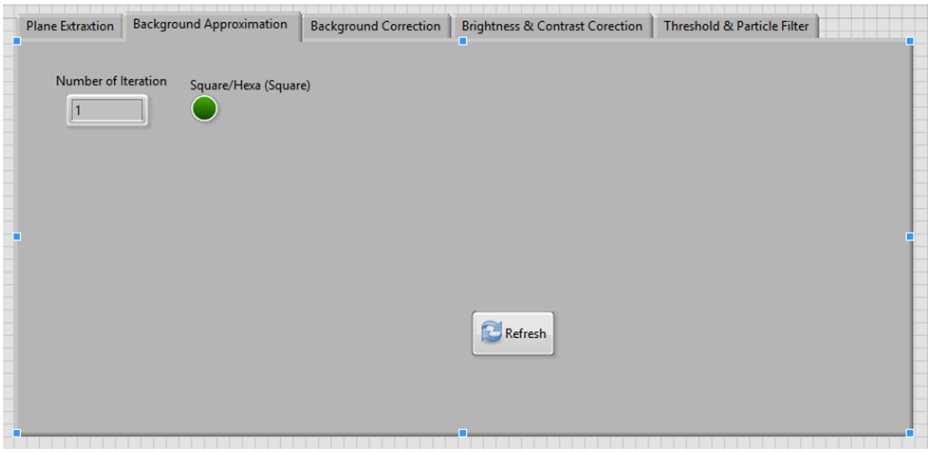

(a) Front panel of add_np_bkaprx.vi

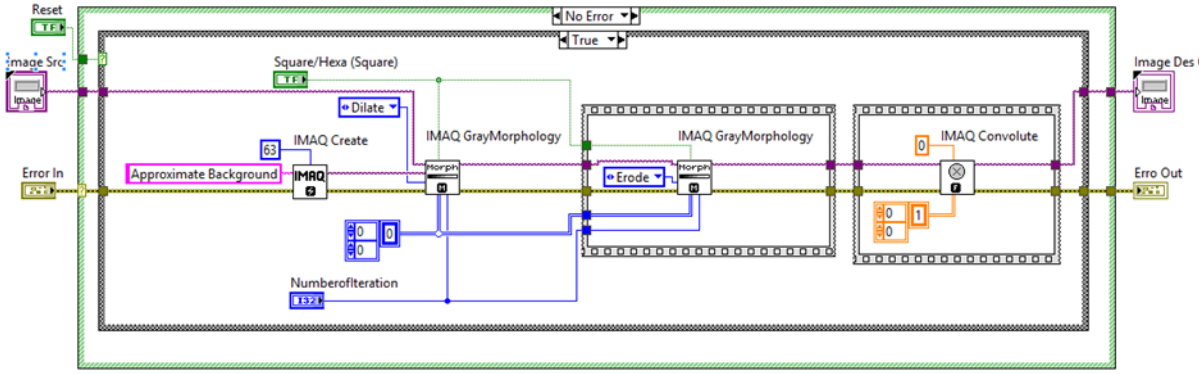

(b) Block diagram of add_np_bkaprx

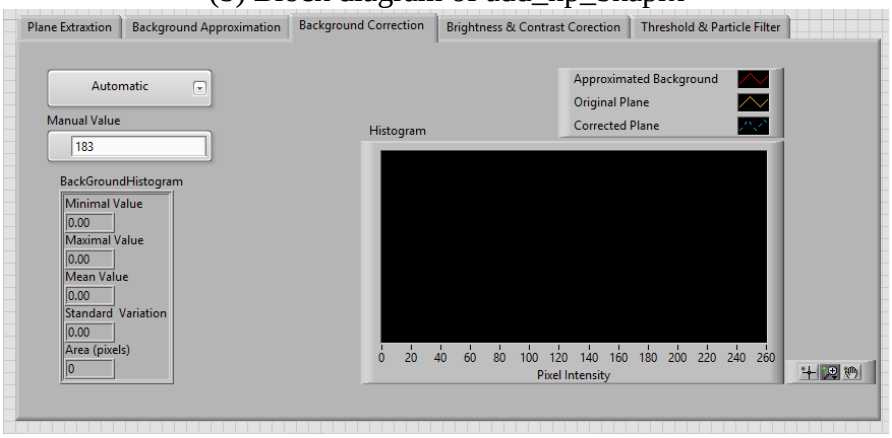

(c) Front panel of add_np_bkcrr.vi

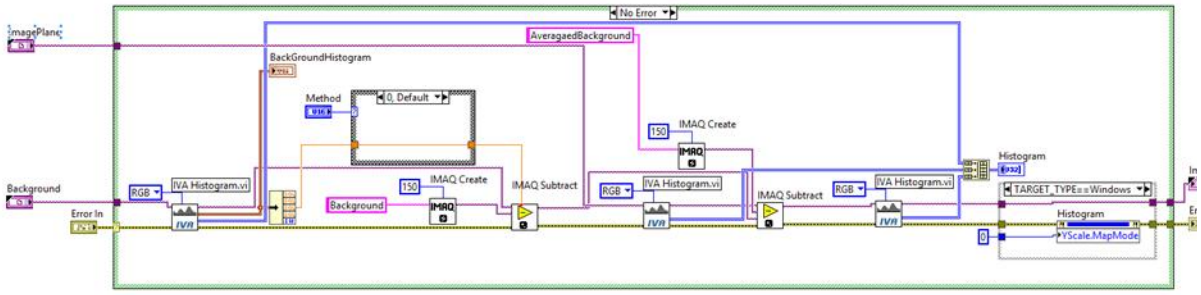

(d) Block diagram of add_np_bkcrr.vi

Figure A-8. The LabVIEW VI for original background approximation and new background correction (add_np.vi/add_np_bkaprx.vi & add_np_bkcrr.vi).

c. <u>Brightness/Contrast/Gama Correction:</u>
(HiberniaImgPro.vi/event structure <Add New Phase >/add_np.vi /add_np_cnstcrr.vi)

As an optional step, the BCG (brightness/contrast/gama) value of the corrected image can changed in this subVI and highlight the aimed phase's regions. Figure A-9 shows the block diagram and front panel of this subVI.

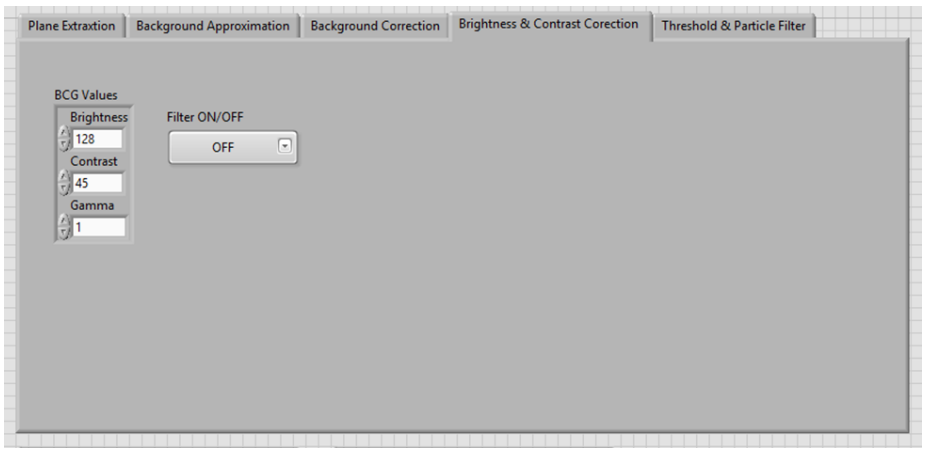

(a)

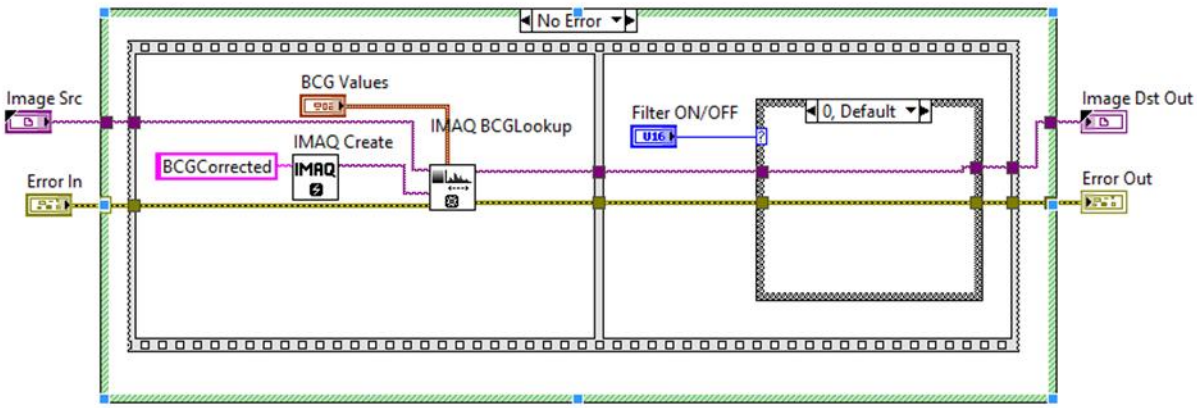

(b)

Figure A-9. The LabVIEW VI for contract enhancement (add_np_cnstcrr.vi).

d. Segmentation:
(HiberniaImgPro.vi/event structure <Add New Phase >/add_np.vi/add_np_thresh.vi)

This subVI thresholds the resulting image from past three modification, and generate a binary image. As Figure A-10 demonstrations, the last function in this subVI's block diagram is the particle analyzer, which identifies and characterize the forming particles thresholded binary image (segmented phase).

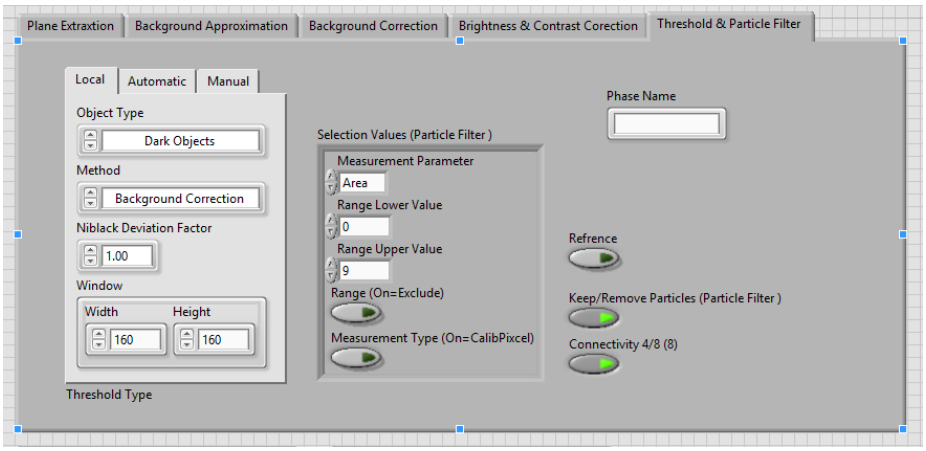

(a) Front panel of add_np_thresh.vi

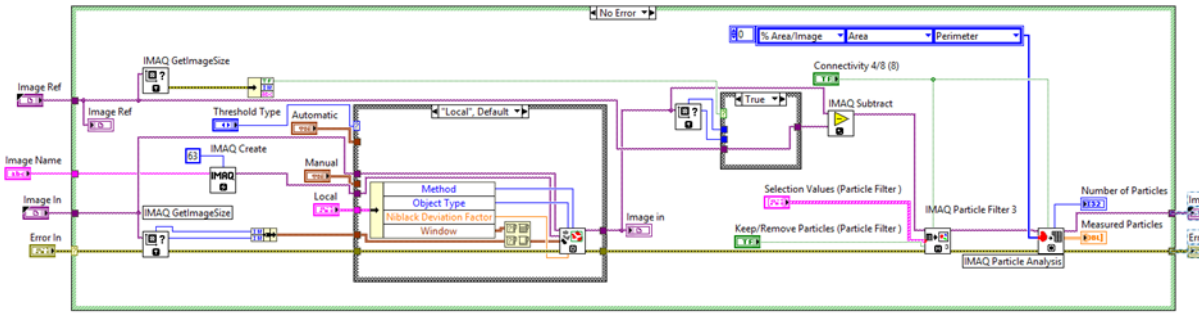

(b) Block diagram add_np_thresh.vi

Figure A-10. The LabVIEW VI for phase segmentation (add_np_thresh.vi).

A.2.3 Batch Calculation

i. Particle calculation:
(HiberniaImgPro.vi/event structure <Calculation Initialization >/cal_numeric.vi)

Following the segmentation subVI (add_np_thresh.vi), the raw properties obtained from particle analysis function can be converted to required parameters, such as saturation, overall perimeter and Uncertainly Thresholded value (UT). The block diagram of these sample calculations is shown in Figure A-11.

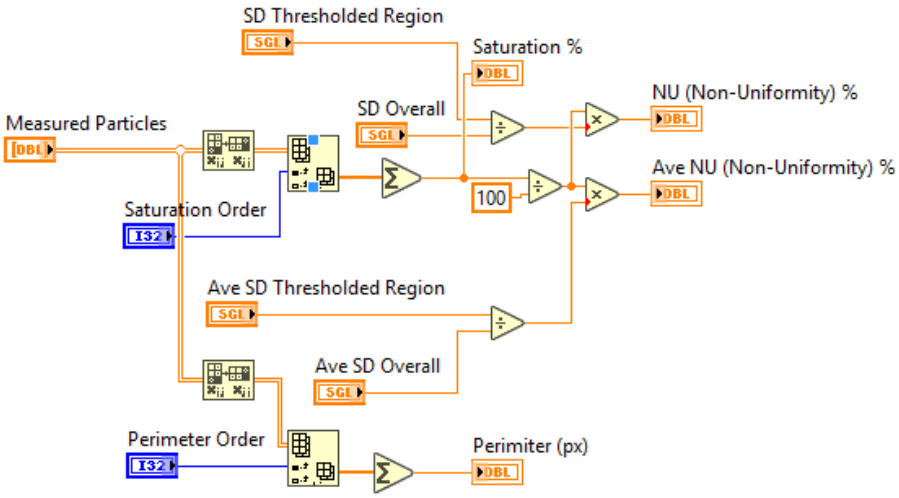

Figure A-11. The block diagram for calculation of image parameters (cal_numeric.vi).

ii. Misclassification Error (ME):
(HiberniaImgPro.vi/event structure <Calculation Initialization >/cal_err3.vi)

As mentioned in section 3.4.1 Thresholding Performance, the misclassified error is a measure that is necessary to optimize the image processing procedure. Therefore in this subVI, as displayed in Figure A-12, the misclassification error associated with the process of three-phase images is calculated.

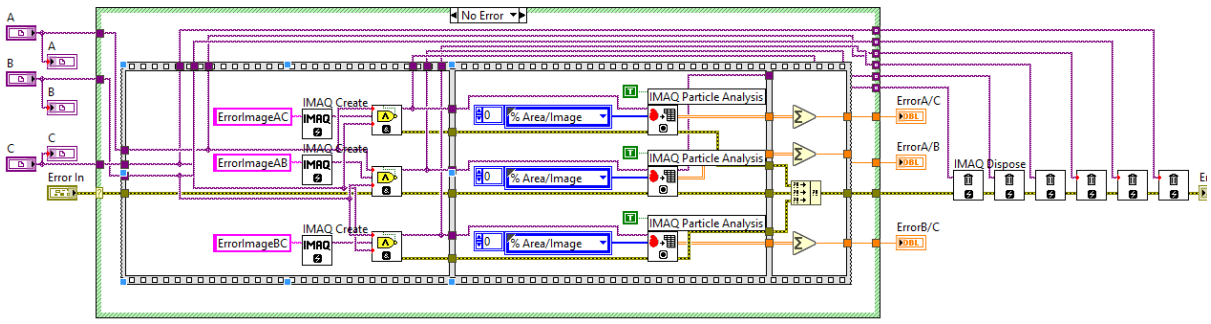

Figure A-12. The block diagram for estimating misclassification error in a three-phase image.

iii. Excel Data Generation:
(HiberniaImgPro.vi/event structure <Calculation Initialization >)

The calculated data from past two subVIs need to be exported to an Excel file. As presented in Figure A-13, the Batch Calculation event structure includes functions for Excel data generator.

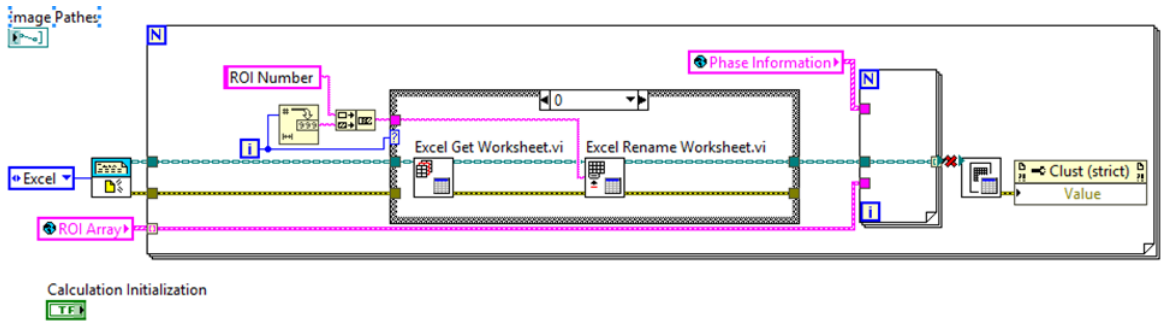

Figure A-13. The structure of exporting data in EXCEL format.

A.3 PCA method sample code in MATLAB

The sample code to extract three principal components from a color image (RGB) is developed in MATLAB as below:

```
I = double(imread('peppers.png'));

X = reshape(I,size(I,1)*size(I,2),3);
```

```
coeff = pca(X);

Itransformed = X*coeff;

Ipc1 = reshape(Itransformed(:,1),size(I,1),size(I,2));

Ipc2 = reshape(Itransformed(:,2),size(I,1),size(I,2));

Ipc3 = reshape(Itransformed(:,3),size(I,1),size(I,2));

figure, imshow(Ipc1,[]);

figure, imshow(Ipc2,[]);

figure, imshow(Ipc3,[]);
```

REFERENCES

[1] A. Al-Adasani and B. Bai, "Recent developments and updated screening criteria of enhanced oil recovery techniques," in *International Oil and Gas Conference and Exhibition in China*, 2010.

[2] A. Muggeridge *et al.*, "Recovery rates, enhanced oil recovery and technological limits," *Phil. Trans. R. Soc. A*, vol. 372, no. 2006, p. 20120320, 2014.

[3] L. Romero-Zerón, "Advances in enhanced oil recovery processes," in *Introduction to Enhanced Oil Recovery (EOR) Processes and Bioremediation of Oil-Contaminated Sites*, InTech, 2012.

[4] D. Tiab and E. C. Donaldson, *Petrophysics: theory and practice of measuring reservoir rock and fluid transport properties*. Gulf professional publishing, 2015.

[5] T. Ahmed and P. McKinney, *Advanced reservoir engineering*. Gulf Professional Publishing, 2011.

[6] A. Satter, G. M. Iqbal, and J. L. Buchwalter, *Practical Enhanced Reservoir Engineering: Assisted with Simulation Software*. PennWell Corporation, 2008.

[7] J. R. Hite, G. Stosur, N. F. Carnahan, and K. Miller, "IOR and EOR: effective communication requires a definition of terms," *J. Pet. Technol.*, vol. 55, no. 6, p. 16, 2003.

[8] F. I. Stalkup Jr, "Status of miscible displacement," *J. Pet. Technol.*, vol. 35, no. 4, pp. 815–826, 1983.

[9] J. R. Christensen, E. H. Stenby, and A. Skauge, "Review of WAG field experience," in *International Petroleum Conference and Exhibition of Mexico*, 1998.

[10] J.-T. Liang, R. L. Lee, and R. S. Seright, "Gel placement in production wells," *SPE Prod. Facil.*, vol. 8, no. 4, pp. 276–284, 1993.

[11] J. J. Sheng, B. Leonhardt, and N. Azri, "Status of polymer-flooding technology," *J. Can. Pet. Technol.*, vol. 54, no. 2, pp. 116–126, 2015.

[12] A. A. Olajire, "Review of ASP EOR (alkaline surfactant polymer enhanced oil recovery) technology in the petroleum industry: Prospects and challenges," *Energy*, vol. 77, pp. 963–982, 2014.

[13] H. Gu *et al.*, "Steam injection for heavy oil recovery: modeling of wellbore heat efficiency and analysis of steam injection performance," *Energy Convers. Manag.*, vol. 97, pp. 166–177, 2015.

[14] GDH, "Applied Petroleum Reservoir Engineering." JSTOR, 1960.

[15] W. C. Lyons and G. J. Plisga, *Standard handbook of petroleum and natural gas engineering*. Gulf Professional Publishing, 2011.

[16] P. C. Smalley, A. W. Ross, C. Brown, T. P. Moulds, and M. J. Smith, "Reservoir technical limits: a framework for maximizing recovery from oil fields," *SPE Reserv. Eval. Eng.*, vol. 12, no. 4, pp. 610–629, 2009.

[17] N. R. Morrow, "Wettability and its effect on oil recovery," *J. Pet. Technol.*, vol. 42, no. 12, pp. 1–476, 1990.

[18] U. G. Araktingi and F. M. Orr Jr, "Viscous fingering in heterogeneous porous media," *SPE Adv. Technol. Ser.*, vol. 1, no. 1, pp. 71–80, 1993.

[19] R. A. Salathiel, "Oil recovery by surface film drainage in mixed-wettability rocks," *J. Pet. Technol.*, vol. 25, no. 10, pp. 1–216, 1973.

[20] M. A. El Ela and H. Sayyouh, "An integrated approach for the application of the enhanced oil recovery projects," *J. Pet. Sci. Res.*, 2014.

[21] J. J. Taber, F. D. Martin, and R. S. Seright, "EOR screening criteria revisited-Part 1:

Introduction to screening criteria and enhanced recovery field projects," *SPE Reserv. Eng.*, vol. 12, no. 3, pp. 189–198, 1997.
[22] R. K. Srivastava, S. S. Huang, and M. Dong, "Comparative effectiveness of CO2 produced gas, and flue gas for enhanced heavy-oil recovery," *SPE Reserv. Eval. Eng.*, vol. 2, no. 3, pp. 238–247, 1999.
[23] R. Farajzadeh, A. Andrianov, R. Krastev, G. J. Hirasaki, and W. R. Rossen, "Foam–oil interaction in porous media: implications for foam assisted enhanced oil recovery," *Adv. Colloid Interface Sci.*, vol. 183, pp. 1–13, 2012.
[24] B. Ju, T. Fan, and M. Ma, "Enhanced oil recovery by flooding with hydrophilic nanoparticles," *China Particuology*, vol. 4, no. 1, pp. 41–46, 2006.
[25] Y. Wang, H. Xu, W. Yu, B. Bai, X. Song, and J. Zhang, "Surfactant induced reservoir wettability alteration: Recent theoretical and experimental advances in enhanced oil recovery," *Pet. Sci.*, vol. 8, no. 4, pp. 463–476, 2011.
[26] P. Zhang, M. T. Tweheyo, and T. Austad, "Wettability alteration and improved oil recovery by spontaneous imbibition of seawater into chalk: Impact of the potential determining ions Ca 2+, Mg 2+, and SO 4 2−," *Colloids Surfaces A Physicochem. Eng. Asp.*, vol. 301, no. 1, pp. 199–208, 2007.
[27] S. M. Ali and S. Thomas, "The promise and problems of enhanced oil recovery methods," *J. Can. Pet. Technol.*, vol. 35, no. 7, 1996.
[28] L. A. James, N. Rezaei, and I. Chatzis, "VAPEX, Warm VAPEX, and Hybrid VAPEX-The State of Enhanced Oil Recovery for In Situ Heavy Oils in Canada," in *Canadian International Petroleum Conference*, 2007.
[29] A. Soudmand-asli, S. S. Ayatollahi, H. Mohabatkar, M. Zareie, and S. F. Shariatpanahi, "The in situ microbial enhanced oil recovery in fractured porous media," *J. Pet. Sci. Eng.*, vol. 58, no. 1, pp. 161–172, 2007.
[30] A. Kantzas, I. Chatzis, and F. A. L. Dullien, "Enhanced oil recovery by inert gas injection," in *SPE Enhanced Oil Recovery Symposium*, 1988.
[31] L. Hendraningrat and L. Shidong, "A glass micromodel experimental study of hydrophilic nanoparticles retention for EOR project," in *SPE Russian Oil and Gas Exploration and Production Technical Conference and Exhibition*, 2012.
[32] T. Austad, S. F. Shariatpanahi, S. Strand, C. J. J. Black, and K. J. Webb, "Conditions for a low-salinity enhanced oil recovery (EOR) effect in carbonate oil reservoirs," *Energy Fuels*, vol. 26, no. 1, pp. 569–575, 2012.
[33] N. Morrow and J. Buckley, "Improved oil recovery by low-salinity waterflooding," *J. Pet. Technol.*, vol. 63, no. 5, pp. 106–112, 2011.
[34] V. A. Lifton, "Microfluidics: an enabling screening technology for enhanced oil recovery (EOR)," *Lab Chip*, vol. 16, no. 10, pp. 1777–1796, 2016.
[35] A. Chatenever and J. C. Calhoun Jr, "Visual examinations of fluid behavior in porous media-part i," *J. Pet. Technol.*, vol. 4, no. 6, pp. 149–156, 1952.
[36] A. Maghzi, A. Mohebbi, R. Kharrat, and M. H. Ghazanfari, "Pore-scale monitoring of wettability alteration by silica nanoparticles during polymer flooding to heavy oil in a five-spot glass micromodel," *Transp. porous media*, vol. 87, no. 3, pp. 653–664, 2011.
[37] A. Emadi and M. Sohrabi, "Visual Investigation of Oil Recovery by LowSalinity Water Injection: Formation of Water Micro-Dispersions and WettabilityAlteration," in *SPE Annual Technical Conference and Exhibition*, 2013.
[38] M. Sohrabi, A. Danesh, D. H. Tehrani, and M. Jamiolahmady, "Microscopic mechanisms of oil recovery by near-miscible gas injection," *Transp. Porous Media*, vol. 72, no. 3, pp. 351–367, 2008.
[39] R. F. Li, W. Yan, S. Liu, G. Hirasaki, and C. A. Miller, "Foam mobility control for surfactant enhanced oil recovery," *SPE J.*, vol. 15, no. 4, pp. 928–942, 2010.

[40] N. K. Karadimitriou and S. M. Hassanizadeh, “A review of micromodels and their use in two-phase flow studies,” *Vadose Zo. J.*, vol. 11, no. 3, 2012.
[41] R. L. Chuoke, P. Van Meurs, and C. van der Poel, “The instability of slow, immiscible, viscous liquid-liquid displacements in permeable media,” 1959.
[42] T. E. Jewell and K. Thompson, “Ringfield lithography.” Google Patents, 24-May-1994.
[43] C. C. Mattax and J. R. Kyte, “Ever see a water flood,” *Oil Gas J*, vol. 59, no. 42, pp. 115–128, 1961.
[44] C. W. Hull, “Apparatus for production of three-dimensional objects by stereolithography.” Google Patents, 11-Mar-1986.
[45] M. A. Unger, H.-P. Chou, T. Thorsen, A. Scherer, and S. R. Quake, “Monolithic microfabricated valves and pumps by multilayer soft lithography,” *Science (80-.).*, vol. 288, no. 5463, pp. 113–116, 2000.
[46] M. W. Wegner and J. M. Christie, “Chemical etching of deformation sub-structures in quartz,” *Phys. Chem. Miner.*, vol. 9, no. 2, pp. 67–78, 1983.
[47] W. G. Johnston, “Dislocation etch pits in non-metallic crystals with bibliography,” *Prog. Ceram. Sci.*, vol. 2, pp. 1–75, 1962.
[48] N. Sagar, L. M. Schlumberger, and W. E. Brigham, “Pore-Level Visualization of Oil/Foam Interactions in a Silicon Micromodel,” *Final Rep. June 1999*, p. 154, 1998.
[49] G. Spierings, “Wet chemical etching of silicate glasses in hydrofluoric acid based solutions,” *J. Mater. Sci.*, vol. 28, no. 23, pp. 6261–6273, 1993.
[50] C. Iliescu, B. Chen, and J. Miao, “On the wet etching of Pyrex glass,” *Sensors actuators A Phys.*, vol. 143, no. 1, pp. 154–161, 2008.
[51] H. Geistlinger, I. Ataei-Dadavi, and H.-J. Vogel, “Impact of Surface Roughness on Capillary Trapping Using 2D-Micromodel Visualization Experiments,” *Transp. Porous Media*, vol. 112, no. 1, pp. 207–227, 2016.
[52] J. Cheng, L. J. Pyrak- Nolte, D. D. Nolte, and N. J. Giordano, “Linking pressure and saturation through interfacial areas in porous media,” *Geophys. Res. Lett.*, vol. 31, no. 8, 2004.
[53] S. T. Wereley and C. D. Meinhart, “Micron-resolution particle image velocimetry,” *Microscale Diagnostic Tech.*, pp. 51–112, 2005.
[54] C. D. Montemagno and W. G. Gray, “Photoluminescent volumetric imaging: A technique for the exploration of multiphase flow and transport in porous media,” *Geophys. Res. Lett.*, vol. 22, no. 4, pp. 425–428, 1995.
[55] H. Hematpour, M. Mardi, S. Edalatkhah, and R. Arabjamaloei, “Experimental study of polymer flooding in low-viscosity oil using one-quarter five-spot glass micromodel,” *Pet. Sci. Technol.*, vol. 29, no. 11, pp. 1163–1175, 2011.
[56] C. J. Kalkman, “LabVIEW: a software system for data acquisition, data analysis, and instrument control,” *J. Clin. Monit.*, vol. 11, no. 1, pp. 51–58, 1995.
[57] A. Korzynska, L. Roszkowiak, C. Lopez, R. Bosch, L. Witkowski, and M. Lejeune, “Validation of various adaptive threshold methods of segmentation applied to follicular lymphoma digital images stained with 3, 3’-Diaminobenzidine&Haematoxylin,” *Diagn. Pathol.*, vol. 8, no. 1, p. 48, 2013.
[58] R. Ramos, R. Zlatev, B. Valdez, M. Stoytcheva, M. Carrillo, and J.-F. García, “LabVIEW 2010 computer vision platform based virtual instrument and its application for pitting corrosion study,” *J. Anal. Methods Chem.*, vol. 2013, 2013.
[59] J. Schindelin *et al.*, “Fiji: an open-source platform for biological-image analysis,” *Nat. Methods*, vol. 9, no. 7, pp. 676–682, 2012.
[60] R. Posada-Gómez, O. O. Sandoval-González, A. M. Sibaja, O. Portillo-Rodríguez, and G. Alor-Hernández, “Digital Image Processing Using LabView,” in *Practical Applications and Solutions Using LabVIEW™ Software*, InTech, 2011.

[61] P. Ferrand, “GPScan. VI: A general-purpose LabVIEW program for scanning imaging or any application requiring synchronous analog voltage generation and data acquisition,” *Comput. Phys. Commun.*, vol. 192, pp. 342–347, 2015.
[62] C. D. Tsakiroglou, M. A. Theodoropoulou, and V. Karoutsos, “Nonequilibrium capillary pressure and relative permeability curves of porous media,” *AIChE J.*, vol. 49, no. 10, pp. 2472–2486, 2003.
[63] M. Riazi, M. Sohrabi, and M. Jamiolahmady, “Experimental study of pore-scale mechanisms of carbonated water injection,” *Transp. porous media*, vol. 86, no. 1, pp. 73–86, 2011.
[64] H. H. Al-Sharji, C. A. Grattoni, R. A. Dawe, and R. W. Zimmerman, “Pore-scale study of the flow of oil and water through polymer gels,” in *SPE Annual Technical Conference and Exhibition*, 1999.
[65] L. Vincent, “Morphological grayscale reconstruction in image analysis: Applications and efficient algorithms,” *IEEE Trans. image Process.*, vol. 2, no. 2, pp. 176–201, 1993.
[66] C. A. Schneider, W. S. Rasband, and K. W. Eliceiri, “NIH Image to ImageJ: 25 years of image analysis,” *Nat. Methods*, vol. 9, no. 7, pp. 671–675, 2012.
[67] W. A. Yasnoff, J. K. Mui, and J. W. Bacus, “Error measures for scene segmentation,” *Pattern Recognit.*, vol. 9, no. 4, pp. 217–231, 1977.
[68] C. Iliescu and E. H. F. Tay, “Wet etching of glass for MEMS applications,” *ROMJIST*, vol. 9, no. 4, pp. 285–310, 2006.
[69] P. Abgrall and A. M. Gue, “Lab-on-chip technologies: making a microfluidic network and coupling it into a complete microsystem—a review,” *J. Micromechanics Microengineering*, vol. 17, no. 5, p. R15, 2007.
[70] Q. Chen, Q. Chen, D. Milanese, and M. Ferraris, “Thermal assisted direct bonding between structured glasses for lab-on-chip technology,” *Microsyst. Technol.*, vol. 15, no. 12, p. 1873, 2009.
[71] Q. Chen, Q. Chen, and M. Ferraris, “Optimization of thermal assisted direct bonding of soda-lime glasses for lab-on chip application,” *Microsyst. Technol.*, vol. 16, no. 4, pp. 527–532, 2010.
[72] M. Stjernström and J. Roeraade, “Method for fabrication of microfluidic systems in glass,” *J. Micromechanics Microengineering*, vol. 8, no. 1, p. 33, 1998.
[73] Q. Chen, Q. Chen, D. Milanese, M. Ferraris, and M. Fokine, “Direct bonding and imprinting techniques for micro-fluidic devices fabrication in commercial soda-lime glass, Patent N,” *TO2007A000345*, 2007.
[74] Q. Chen, D. Milanese, Q. Chen, M. Ferraris, and G. C. Righini, “Fabrication and direct bonding of photosensitive multicomponent silicate glasses for lossless planar waveguide splitters,” *J. Non. Cryst. Solids*, vol. 354, no. 12, pp. 1230–1234, 2008.
[75] I. Fazal, E. Berenschot, H. Jansen, and M. Elwenspoek, “Bond strength tests between silicon wafers and Duran tubes (fusion bonded fluidic interconnects),” in *Solid-State Sensors, Actuators and Microsystems, 2005. Digest of Technical Papers. TRANSDUCERS’05. The 13th International Conference on*, 2005, vol. 1, pp. 936–939.
[76] A. Sayah, D. Solignac, T. Cueni, and M. A. M. Gijs, “Development of novel low temperature bonding technologies for microchip chemical analysis applications,” *Sensors Actuators A Phys.*, vol. 84, no. 1, pp. 103–108, 2000.
[77] M. McKellar and N. C. Wardlaw, “A method of making two-dimensional glass micromodels of pore systems,” *J. Can. Pet. Technol.*, vol. 21, no. 4, 1982.
[78] M. Itano, F. W. Kern, M. Miyashita, and T. Ohmi, “Particle removal from silicon wafer surface in wet cleaning process,” *IEEE Trans. Semicond. Manuf.*, vol. 6, no. 3, pp. 258–267, 1993.
[79] S. Bélanger, “Drilling Holes in Clear Flat Plate Glass Using a Drill Press. in The 61th

Annual ASGS Symposium 2016," 2016.
[80] M. Sohrabi, D. H. Tehrani, A. Danesh, and G. D. Henderson, "Visualization of oil recovery by water-alternating-gas injection using high-pressure micromodels," *SPE J.*, vol. 9, no. 3, pp. 290–301, 2004.
[81] Q. Feng, L. Di, G. Tang, Z. Chen, X. Wang, and J. Zou, "A visual micro-model study: The mechanism of water alternative gas displacement in porous media," in *SPE/DOE Symposium on Improved Oil Recovery*, 2004.
[82] D. B. Weibel and G. M. Whitesides, "Applications of microfluidics in chemical biology," *Curr. Opin. Chem. Biol.*, vol. 10, no. 6, pp. 584–591, 2006.
[83] H. Khajepour, M. Mahmoodi, D. Biria, and S. Ayatollahi, "Investigation of wettability alteration through relative permeability measurement during MEOR process: A micromodel study," *J. Pet. Sci. Eng.*, vol. 120, pp. 10–17, 2014.
[84] M. Sohrabi, A. Emadi, S. A. Farzaneh, and S. Ireland, "A thorough investigation of mechanisms of enhanced oil recovery by carbonated water injection," in *SPE Annual Technical Conference and Exhibition*, 2015.
[85] M. Wirth, M. Fraschini, M. Masek, and M. Bruynooghe, "Performance evaluation in image processing," *EURASIP J. Appl. Signal Processing*, vol. 2006, p. 211, 2006.
[86] J. Gauch and C.-W. Hsia, "A comparison of three color image segmentation algorithms in four color spaces," in *Visual Communication and Image Processing*, 1992, vol. 1818, pp. 1168–1181.
[87] M. T. Orchard and C. A. Bouman, "Color quantization of images," *IEEE Trans. signal Process.*, vol. 39, no. 12, pp. 2677–2690, 1991.
[88] E. Littmann and H. Ritter, "Adaptive color segmentation-a comparison of neural and statistical methods," *IEEE Trans. neural networks*, vol. 8, no. 1, pp. 175–185, 1997.
[89] J. Kender, H. Saturation, and N. Color, "Calculation, Digitization Effects and Use," *Tech. Report, Dept CS, Carnegie-Mellon Univ.*, 1976.
[90] R. A. Schowengerdt, *Techniques for image processing and classifications in remote sensing*. Academic Press, 2012.
[91] K. Karhunen, *Über lineare Methoden in der Wahrscheinlichkeitsrechnung*, vol. 37. Universitat Helsinki, 1947.
[92] M. Loeve, "Probability theory, 3rd éd," *New York*, 1963.
[93] D. L. Omucheni, K. A. Kaduki, W. D. Bulimo, and H. K. Angeyo, "Application of principal component analysis to multispectral-multimodal optical image analysis for malaria diagnostics," *Malar. J.*, vol. 13, no. 1, p. 485, 2014.
[94] Y.-I. Ohta, T. Kanade, and T. Sakai, "Color information for region segmentation," *Comput. Graph. image Process.*, vol. 13, no. 3, pp. 222–241, 1980.
[95] P. Singh and A. K. Garg, "Non Uniform Background Removal using Morphologybased Structuring Element for Particle Analysis," *Int. J. Comput. Appl.*, vol. 33, no. 6, pp. 11–16, 2011.
[96] M. Kowalczyk, P. Koza, P. Kupidura, and J. Marciniak, "Application of mathematical morphology operations for simplification and improvement of correlation of images in close-range photogrammetry," *Int. Arch. Photogramm. Remote Sens. Spat. Inf. Sci.*, vol. 37, pp. 153–158, 2008.
[97] H.-D. Cheng, X. H. Jiang, Y. Sun, and J. Wang, "Color image segmentation: advances and prospects," *Pattern Recognit.*, vol. 34, no. 12, pp. 2259–2281, 2001.
[98] D. A. Navastara and A. Z. Arifin, "Image Thresholding on Segmentation of Teeth in Dental Panoramic Radiographs," in *di dalam Proceeding of The International Conference on Advanced Computer Science and Information System*, 2009.
[99] M. Sezgin, "Survey over image thresholding techniques and quantitative performance evaluation," *J. Electron. Imaging*, vol. 13, no. 1, pp. 146–168, 2004.

[100] N. Otsu, “A threshold selection method from gray-level histograms,” *IEEE Trans. Syst. Man. Cybern.*, vol. 9, no. 1, pp. 62–66, 1979.
[101] C. H. Li and C. K. Lee, “Minimum cross entropy thresholding,” *Pattern Recognit.*, vol. 26, no. 4, pp. 617–625, 1993.
[102] W. Niblack, *An introduction to digital image processing*. Strandberg Publishing Company, 1985.
[103] W.-H. Tsai, “Moment-preserving thresolding: A new approach,” *Comput. Vision, Graph. Image Process.*, vol. 29, no. 3, pp. 377–393, 1985.
[104] T. Klinger, *Image processing with LabVIEW and IMAQ Vision*. Prentice Hall Professional, 2003.
[105] X. Shen and J. P.-Y. Maa, “A camera and image processing system for floc size distributions of suspended particles,” *Mar. Geol.*, vol. 376, pp. 132–146, 2016.